UNIVERSITY OF OKLAHOMA

GRADUATE COLLEGE

ESTIMATING BRITTLENESS USING SEISMIC DATA IN AN UNCONVENTIONAL SHALE RESERVOIR, FORT WORTH BASIN, NORTH CENTRAL TEXAS

A THESIS

SUBMITTED TO THE GRADUATE FACULTY

in partial fulfillment of the requirements for the

Degree of

MASTER OF SCIENCE

By

MEGAN JO GUNTHER
Norman, Oklahoma
2017

ESTIMATING BRITTLENESS USING SEISMIC DATA IN AN UNCONVENTIONAL SHALE RESERVOIR, FORT WORTH BASIN, NORTH CENTRAL TEXAS

A THESIS APPROVED FOR THE
CONOCOPHILLIPS SCHOOL OF GEOLOGY AND GEOPHYSICS

BY

_____
Dr. Kurt Marfurt, Chair

_____
Dr. John Pigott

_____
Dr. Matthew Pranter

To my mother and granmom, you have been my powerhouse throughout my life and throughout my graduate career. Thank you for teaching me that hard work, regardless of gender and race, can get you anywhere.

Acknowledgements

Thank you to the AASPI consortium for the continued support throughout this research. Additionally, I would like to thank Pioneer Natural Resources for providing the data for this study.

I would also like to acknowledge all those individuals that helped guide me throughout my graduate studies. Dr. Marfurt, thank you for believing in me and giving me a chance to study under your help and guidance; it hasn't always been easy but it has been a fun adventure. Dr. John Pigott, thank you for your unique help and guidance in not only in geology but also in life; thank you for not only being my professor and mentor but for also allowing me to call you a friend. Dr. Matthew Pranter, thank you for all your help throughout my research and for being an excellent educator; the amount of work you put into everything you do is inspiring.

To my fellow classmates and research group, each of you have inspired me and taught me so much throughout my time at the University of Oklahoma. Ishank Gupta thank you for your guidance and support in areas of studies that I was not familiar with that eventually became a great part of my research, it was not only educational but a whole lot of fun working with you and I am glad to call you my friend, and thanks for the curry! Lennon Infante thank you for your geologic and quantitative interpretation help, the knowledge you carry around is extraordinary. Benmadi thank you for your help and support throughout my research, it was great being able to bounce ideas off of you. Everyone not only encouraged me during times when I was sure I would not succeed but gave me one heck of a time during these last two years. Lastly, I would like to thank

my partner in crime on this project, Swetal Petal, it was a joy to work with you and an honor to call you my friend.

Lastly, to my friends, and boyfriend, thanks for being individualistic, encouraging, smart, entertaining, and accepting of others it truly is inspiring to be surrounded by great people.

Table of Contents

Acknowledgements iv

List of Tables viii

List of Figures ix

Abstract xiv

Chapter 1: Introduction 1

Chapter 2: Geologic Background 4

Regional Geology 4

Barnett Shale 5

Chapter 3: Methods 13

Brittleness 13

Seismic Interpretation 14

Brittleness Average 15

Total Organic Carbon (TOC) and its influence on Brittleness 16

λρ and μρ 17

Prestack Seismic Inversion 18

Microseismic Data 20

Fracture Detection Using Borehole Image Logs 21

Curvature Attribute 21

Brittleness Classification Volume 22

Study Limitations 22

Chapter 4: Results 42

Young's Modulus and Poisson's Ratio Cross Plots 42

TOC and Brittleness Affects 42
λρ-μρ Crossplots 42
λρ and μρ from Seismic Prestack Inversion 43
Validating Brittleness Estimations with Microseismic 44
Borehole Image Logs 46
Fracture Association with the Curvature Attribute 46
Curvature Association with the Microseismic Events 47
Brittleness Classification 48
Chapter 5: Conclusions 68
References 70
Appendix 74
Amplitude versus Offset (AVO) 74

List of Tables

Table 3. 1: λρ, μρ, Young's Modulus, and Poisson's Ratio values for the three most common pure minerals within the Barnett Shale by (Mavko, et al., 2009)..... 31

List of Figures

Figure 1. 1: Cross-Plot of Poisson's ratio and Young's modulus indicating brittle and ductile regions (Grieser and Bray, 2007). 3

Figure 2. 1: Shale plays within the United States lower 48. Black arrow shows the area of study, Fort Worth Basin, for this project (EIA, 2011). 9

Figure 2. 2: Generalized stratigraphic column of the northerns portion of the Fort Worth Basin showing significant formations (Bowker, 2007). 10

Figure 2. 3: Areal extent of the Barnett Shale within the Fort Worth Basin based on hydrocarbon production. The red star indicates the area of study (Montgomery et al., 2005). 11

Figure 2. 4: Generalized stratigraphic column of the Fort Worth Basin and Barnett Shale with approximate well location used in this study (courtesy of Pioneer Natural Resources). 12

Figure 3. 1: Stages of deformation with increasing stress. 24

Figure 3. 2: Map view showing well 4P used in this study relative to Perez and Marfurt (2013) study wells. 25

Figure 3. 3: Depth structure maps of the top (a) Caddo, (b) Marble Falls, (c) Barnett, (d) Forestburg, (e) Lower Barnett, (f) Barnett Hardshale, (g) Base Barnett Unconformity, (h) Ellenburger formations. Yellow arrows indicate karst collapse features in the Ellenburger. 26

Figure 3. 4: (a) Variance attribute extracted along the top Ellenburger horizon slice. (b) Variance horizon slice with amplitude in the vertical section. Yellow arrow indicates

the karst collapse feature corresponding to a bowl like shape in the amplitude section and the edge shown by the variance. 27

Figure 3. 5: Stress-strain diagram of a rock volume subjected to increasing stress, the slope of the linear portion of the line intersecting the origin is Young's Modulus. The steeper the slope the larger Young's modulus. 28

Figure 3. 6: Poisson's ratio is the measurement of the expansion of a material divided by the axial compression ($\varepsilon_1/\varepsilon_2$). The larger the Poisson's ratio, the more brittle a material. The average Poisson's ratio for the three main minerals in the Barnett are given by: Quartz= 0.064, Clay= 0.14, Calcite= 0.3. 29

Figure 3. 7: Calculated geomechanical properties from well logs. Track 7 and 8, Poisson's ratio and Young's modulus, are crossploted against each in Figures 5.1, 5.2, and 5.3. Track 9 is TOC calculated using Passey's equation. 30

Figure 3. 8: Average phase of the prestack seismic data used for the seismic inversion. 32

Figure 3. 9: Seismic data to well tie. The red horizontal lines are the formation tops used to compute the well-tie using the measured gathers. To the left of the blue line are the offsets that were considered for this study and to the right are offsets that were muted (>30 degrees) (discussed in Appendix A). 33

Figure 3. 10: Wavelet extracted from the 4P well for the angle limited stacks. The wavelets are extracted for angles 0-10, 11-20, 21-30, and all angles combined with amplitude ranges from -25 to 50. 34

Figure 3. 11: Misfit between the modeled and measured gathers. The error is the difference between the two. 35

Figure 3. 12: (a) Variance extracted along the Base Barnett Unconformity formation. Yellow arrow indicates a karst collapse feature, (b) Calculated average P impedance from the top of the Barnett to the top of the Base Barnett Unconformity formation. Yellow arrow indicates a high anomalous impedance in a karst collapse feature, (c) Calculated average S impedance from the top of the Barnett to the top of the Base Barnett Unconformity formation. 36

Figure 3. 13: (A) Crossline section through the anomalous P-impedance area. Black box indicates an increase in P-impedance where karst collapse feature is located. This anomaly is due to thicker bedforms containing increased biogenic quartz content resulting in a decrease in porosity, therefor an increase in density, resulting in an increase in P-impedance. (B) Variance extracted along the Base Barnett Unconformity, (C) Average P-impedance of the Barnett shale 37

Figure 3. 14: Median relative error from the prestack data inversion from the top of the Upper Barnett to the top of the Base Barnett Unconformity. 38

Figure 3. 15: (a) 2D colorbar with mineral ternary diagram lying in the $\lambda\rho$ and $\mu\rho$ space, (b) 2D data histogram with mineral ternary diagram in the $\lambda\rho$ and $\mu\rho$ space. Colorbar is clipped to fit data shown by the 2D histogram. 39

Figure 3. 16: Mohr circle diagram. Mohr circle shifts left when fluid injected. σ_1 is the maximum effective stress and σ_3 is the minimum effective stress, and P is the pressure of the fluid. 40

Figure 3. 17: Schematic 2D section of a curved surface featuring anticlinal and synclinal structures. Positive curvature is defined as anticlinal features while negative curvature is

defined as synclinal features. The curvature (k) is defined by 1/r, where r is the radius of the circle that is tangent and fits to each point of the curve (Roberts, 2001). 41

Figure 4. 1: Young's Modulus versus Poisson's ratio plots. (A) All formations in the study. Where the red circle indicates limestone formations while the blue circle indicates shale formations, (B) All formations plotted against Perez and Marfurt's (2013) brittleness template. 49

Figure 4. 2: (a) Perez and Marfurt's (2013) TOC values with the overlaying ternary diagram, (b) Modeled TOC values for all formations, (c) Modeled TOC values for only the Barnett Shale. Red circle indicates the Barnett Hardshale, orange circle indicates the Lower Barnett, and the blue circle indicates the Upper Barnett. (d) Modeled TOC of the Upper Barnett, Lower Barnett, and Barnett Hardshale formations overlaid with the ternary diagram. 50

Figure 4. 3: (A) λρ-μρ crossplots of all formations, (B) λρ-μρ crossplot for Barnett, Lower Barnett, Barnett Hardshale, and Base Barnett Unconformity with the ternary diagram of the three most common minerals within the Barnett Shale. 51

Figure 4. 4: Vertical slices along line AA' through (A) μρ (B) λρ. The well displays gamma ray. 52

Figure 4. 5: (A) 2D color bar with the ternary diagram in the λρ-μρ space, (B) 2D histogram of the data. The white dashed box indicates where the data has been clipped in the following Figures. 53

Figure 4. 6: Vertical slice BB' through the λρ-μρ cross plot displayed with th gamma ray log from well 4P. Limestone formations appears as purple colors while the shale formations appears as green and yellow colors. 54

Figure 4. 7: Arial view of the pilot well 4P and the deviated well 2H with its corresponding microseismic events. Different colors represent the 13 different stages 55
Figure 4. 8: Vertical slice CC' through the λρ-μρ volume along the horizontal path of well 2H, showing the 13 stages of microseismic events corresponding to well 2H. The dashed boxes shows the stages in which the microseismic events are less clustered and propagate into the overlying limestone Forestburg formation. 56
Figure 4. 9: λρ and μρ values [(GPa)(g/cm^3)] extracted at each microseismic event location for all stages along with the brittleness template and ternary diagram of the three most common minerals in the Barnett Shale. 57
Figure 4. 10: λρ and μρ values [(GPa)(g/cm^3)] extracted at each microseismic event location for the first five stages along with the brittleness template and ternary diagram of the three most common minerals in the Barnett Shale. 58
Figure 4. 11: (A) Vertical slice through the λρ-μρ volume with the image log plotted along the borehole of well 2H. White box indicates a zone of more open fractures. (B) Same as A with added microseismic events. 59
Figure 4. 12: Amplitude data co-rendered with most positive curvature in the vertical seismic section and energy ratio similarity co-rendered with most positive curvature in a time slice. Well 2H displaying the fracture type on the horizontal section of the well. Open fractures are more abundant where a positive curvature anomaly exists. 60
Figure 4. 13: (A) Vertical slice through the most positive curvature co-rendered with seismic amplitude volumes along with well 2H with the corresponding fracture type from image logs, (B) Vertical section of the most positive curvature attribute co-rendered with seismic amplitude along with the 13 stages of microseismic. Black box

indicates an area with high open and partially open fracture intensity and un-clustered microseismic events. 61

Figure 4. 14: Quantitative analysis of open fractures with associated most positive curvature values. 62

Figure 4. 15: Quantitative analysis of the most positive curvature attribute values for each associated microseismic events. 63

Figure 4. 16: Depth slice of most positive curvature and energy ratio similarity showing the shallower microseismic events. Notice, events avoid areas of higher values of curvature (yellow arrows) and act as fracture barriers and cluster towards lower values and negative dome like features. 64

Figure 4. 17: Brittleness classification seismic volume. (a) brittleness classification volume with the well 2H path, (b) same as (a) with the added microseismic events and a close-up section of the microseismic events, (c) horizon slice of the Barnett Hardshale with the well 2H deviated path, (d) same as (c) with the added microseismic events. Many of the events are clustered within the brittle and less brittle zones except for stages 7-14 highlighted by the blue circle which appear in the ductile Forestburg Limestone. 65

Figure 4. 18: Extracted brittleness classification for every stage of microseismic events at every event location. 66

Figure 4. 19: Extracted brittleness classification for stages 2-6 of microseismic events at every event location. 67

Figure A 1: AVO curve for the top Marble Falls formation demonstrating a type 1 AVO effect. 76
Figure A 2: AVO curve for the Caddo formation. Caddo event is a strong peak across all offsets. The blue box indicates an anomalous area due to near and far offset event not aligned and approaching zero crossing at far offsets, possibly due to slow velocity picks. 76
Figure A 3: AVO curve for the top Barnett Shale, the blue box indicates an anomalous area. 77
Figure A 4: AVO curve for the Forestburg formation. The blue box indicates an area of interest within the Forestburg formation. 77
Figure A 5: AVO curve for the Lower Barnett. The blue box indicates possible tuning effects within the Lower Barnett formation. 78
Figure A 6: AVO curve for the Barnett Hardshale formation. 78
Figure A 7: AVO curve for the Base Barnett Unconformity formation. 79
Figure A 8: AVO curve for the Ellenburger formation. 79

Abstract

Brittleness within unconventional shale plays is a major component in reservoir stimulation. Mineralogy measured in nearby wells estimates brittleness and can be correlated to elastic parameters measured in well logs and surface seismic data. Brittle zones are dominated by high quartz and TOC while ductile zones are dominated by clay and calcite with lower TOC. $\lambda\rho$ and $\mu\rho$ calculated from prestack inversion seismic data predictes brittle and ductile zones, which is validated using microseismic data. Near the heel of the well, many microseismic events propagated into the more ductile Forestburg limestone. Using a borehole image log, it appears that open and partially open fractures allow perforation energy to travel into the overlying more ductile formations. Near the toe of the well events occur in the more brittle areas of the target Barnett Shale formation. Correlating fracture type with curvature, low (near zero) values of most positive curvature are highly fractured and contains the most microseismic activity. Creating a brittleness volume, microseismic events occur in brittle and less brittle zones with the exception of the events that occur in the ductile Forestburg limestone due to an increase in open and partially open fractures towards the heel of the well.

Chapter 1: Introduction

Most conventional petroleum systems consist of a separate source, seal, and reservoir. Hydrocarbons generation begins with an organic rich rock subjected to high temperatures at depth, oil and gas is expulsed and migrates to a porous reservoir rock and is trapped by an impermeable seal. In contrast to conventional reservoirs, unconventional shale reservoirs where the source, seal, and reservoir are in the same rock having little to no permeability. To produce the hydrocarbons from the reservoir special recovery methods, such as hydraulic fracturing, is needed to create the necessary permeability.

The majority of the production in the Barnett Shale comes from zones that are high in quartz and lower in clay (Bowker, 2003). He also shows the Barnett Shale has an average porosity of 6%. The identification of brittle from ductile zones is key to stimulation success within shale-gas plays. Several methods to estimate brittleness have been defined with not one method being a universal method. Jarvie et al. (2007), define brittleness to be controlled by mineralogy: clay, calcite, quartz, and TOC. Javie et al.'s (2007) brittleness index provides a smooth transition between brittle and ductile regions. In contrast, Grieser and Bray (2007) define brittle and ductile regions based on Poisson's ratio and Young's modulus, and provide an empirical template for the Barnett Shale (Figure 1.1).

The use and combination of seismic data, well log information, and seismic attributes are commonly used to create maps of hydrocarbon reservoirs. These maps can be used to identify potential drilling hazards such as karsts features that are frequently found in carbonate rocks (Sullivan et al., 2006) as well as brittle zones within an existing reservoir for better recovery methods.

The objective of this thesis is to identify brittle from ductile zones within the Barnett Shale from the use and combination of seismic and well log data. Beginning with mapping the formations of interest to gain a broad understanding of the regional geology in the area of study. The geomechanical properties will be calculated and plotted against Perez (2013) brittlness template. Followed by, a seismic prestack inversion to calculate the $\lambda\rho$ and $\mu\rho$ using the impedance volumes to estimate brittleness and mineralogy. Estimations will be validated using thirteen stages of microseismic events and the event behavior along the lateral portion of the well will be investigated using an image log to correlate fracture types with most positive curvature. Using Perez's (2013) brittleness template, a brittleness volume for the Barnett Shale and validated with microseismic events. I quantify my results using histograms to correlate fracture type, curvature, $\lambda\rho$-$\mu\rho$, and brittleness classification at each microseismic event location. Microseismic events occur in the more brittle and less brittle areas with the exception of those events in the more ductile Forestburg formation, due to an abundance of open and partially open fractures.

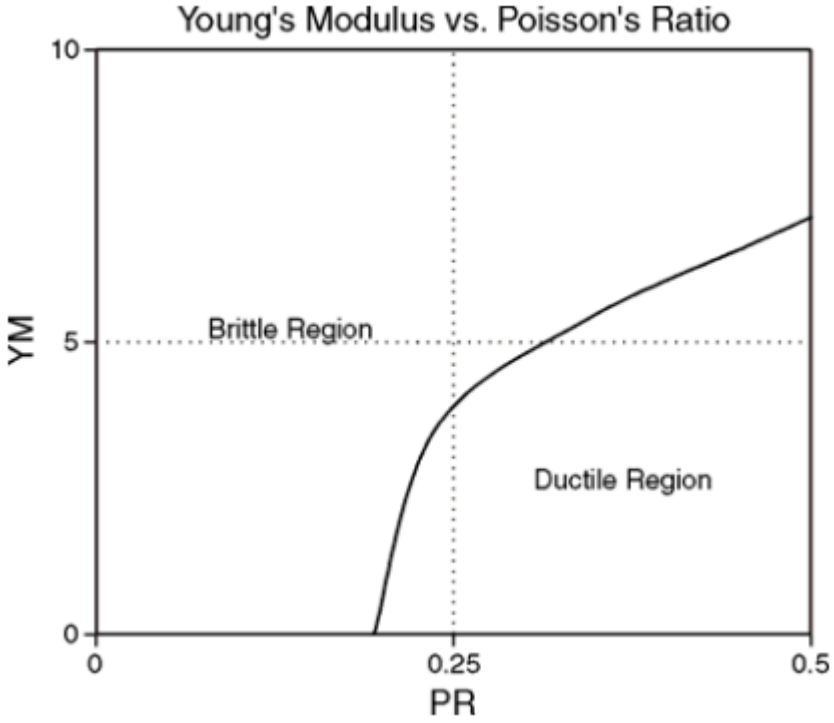

Figure 1. 1: Cross-Plot of Poisson's ratio and Young's modulus indicating brittle and ductile regions (Grieser and Bray, 2007).

Chapter 2: Geologic Background

Regional Geology

The Fort Worth Basin is a N-S trending foreland basin with an area of 15,000 mi^2 in north Texas and southwestern Oklahoma which formed during the late Paleozoic Ouachita orogeny during the formation of Pangea (Montgomery et al., 2005) (Figure 2.1). The Fort Worth Basin is an asymmetrical wedge shaped basin bounded by the Ouachita structural front to the east, Llano uplift to the south, Red River and Muenster Archs to the north, and the Bend arch to the west.

Montgomery et al., (2005) observed that the major structural features located within the Fort Worth Basin include major and minor faulting, local folding, karst collapse features within the carbonate Ellenburger, fractures associated with fault trends, and fracture fills with carbonate cement. Another significant structural element present within the Fort Worth Basin is the Mineral Wells fault, a basement feature that experienced periodic rejuvenation in the late Paleozoic. The Mineral Wells fault bisects the Newark field, the most prolific hydrocarbon field within the Fort Worth Basin, and influences depositional patterns, thermal history, and migration pathways within the Barnett Shale (Montgomery et al., 2005).

The Fort Worth Basin contains several significant formations including the Ellenburger, Viola and Simpson, Barnett Shale (Lower and Upper), Forestburg, Marble Falls, and Caddo (Figure 2.2). The Ellenburger is a carbonate formation with karst collapse features, with associated breccias and fractures, that developed during a drop in sea level resulting in platform exposure and extensive karst-related deposits (Kerans, 1988). Overlying the Ellenburger is the erosional Viola and Simpson formations characterized by dense,

crystalling and dolomitic limestone confined to the northeastern part of the basin. Above the erosional surface are the Mississippian deposits with alternating sequences of shallow marine limestones and organic rich shales known as the Barnett Shale. The Barnett Shale is broken up into two sections, Lower and Upper Barnett Shale, that are separated by the Forestburg limestone (Montgomery et al., 2005). The Lower Barnett Shale contains higher Quartz content compared to the Upper Barnett that has higher carbonate content (Perez, 2013). This study is focused on the Barnett Shale formation.

Barnett Shale

The Mississippian Barnett formation located in the Fort Worth Basin is an unconventional shale gas play where the source, reservoir, and seal is all located within the same formation. Though there is continued debate as to how the Barnett was deposited, for this paper we will assume the strata was deposited in a deep-water system with poor circulation that allowed for the accumulation of organic matter. Barnett deposition is estimated to have occurred over a 25-million-year period with the source of sedimentation coming from debris transported to the basin from the shelf or upper oxygenated slope by hemipelagic mud plumes, dilute turbidites, and debris flows. Most of the sedimentation in the Fort Worth Basin of Mississippian age comes from the Chappel Shelf (carbonates) to the West and the Caballos Arkansas island chain to the south (terrigenous) (Loucks et al., 2007).

Figure 2.3 shows the primary structural elements of the Barnett Shale within the Fort Worth Basin. The Barnett shale is bounded by the Muenster arch on the Northeast, Ouachita thrust belt in the Southeast, Llano Uplift northern extension bend arch to the West, and Red River Uplift to the North. Based on Montgomery et al., (2005) the major

structural elements include faults on various scales, folds, fractures related to faulting, and karst collapse features.

The Barnett Shale is one of the world's most prolific unconventional shale gas plays and is located in northern Texas. Though it has long been recognized as a probable source rock for hydrocarbons, prior to the 1980's the Barnett Shale was not a target for hydrocarbon exploration. However, owing to unexpected gas shows and production from the Barnett Shale convinced Mitchell Energy and Development Corp. to explore the shale formation as a possible hydrocarbon reservoir. The low permeability of the tight shale rock resulted in uneconomic production within the Barnett. With the continued progression of engineering practices and completion techniques resulted in an economic hydrocarbon formation (Montgomery et al., 2005).

According to Schmoker et al. (1996); and Pollastro (2003) the Barnett Shale is interpreted as a continuous natural gas accumulation in the Fort Worth basin. Zuo et al., 2013 defines a continuous natural gas accumulation reservoir as an unconventional reservoir with continuous distributed hydrocarbons that make up a large proportion of an unconventional reservoir system. Much of the production is in Newark East field ($400mi^2$) where the formation ranges from 300-500ft in thickness and gas saturation of about 75% at depths of 6500-8500ft. Bounding the Barnett shale stratigraphically is the overlying carbonate, Marble Falls group, and underlying the formation is the carbonate Ellenburger group that is heavily karsted. Separating the Lower and Upper Barnett is the Forestburg limestone. These bounding limestone formations (Marble Falls, Forestburg, and Ellenburger) act as fracture barriers when the formation is hydraulically fractured.

The stratigraphic units of interest for this study are Mississippian in age and is shown in Figure 2.4 which is a generalized stratigraphic section of the Barnett shale with over and underlying formations. A more detailed section is also shown in Figure 2.3 with the approximate well location used for this study. The Barnett section is broken up into three different units. These units include the Upper Barnett, Lower Barnett, and Forestburg limestone. Above the Barnett Shale is the Marble Falls and Caddo limestone formations, and beneath the Lower Barnett is the Base Barnett Unconformity and the Ellenburger which is a carbonate formation of Ordovician age that has an abundance of karst features due to subaerial exposure during a time of low sea level.

According to Perez's (2013) study using seven elemental capture spectroscopy (ECS) logs, the Lower Barnett Shale has higher quartz content compared to the Upper Barnett Shale. Perez also found that the Forestburg was dominated by calcite with a signature low gamma ray response compared to the Lower and Upper Barnett.

The Barnett shale is a unique shale-gas play for a multitude of reasons. First, the Barnett shale is highly heterogeneous therefore should not be thought of as a "blanket" depositional environment with clay, quartz, and carbonate as the dominant mineral (Karastathis, 2007). Because of this heterogeneity, some areas are more brittle compared to other areas and therefore fracture much easier during stimulation. Second, the production from within the Barnett are at greater depths therefore higher pressures compared to other shale-gas reservoirs. Third, natural fractures do not appear to be essential for production within the Barnett shale and in some cases, hinder the well performance. The uniqueness of the Barnett has resulted in many challenges amongst

geoscientists and engineers whose primary focus is to characterize and produce from the Barnett Shale reservoir (Montgomery et al, 2005).

As stated before to enhance recovery in unconventional shale plays hydraulic fracturing is performed to create and reopen preexisting fracture networks that create sweet spots for hydrocarbon accumulation. Horizontal drilling and hydraulic fracturing has greatly increased the recovery and profitability of these low permeability shale gas plays. However, fracture locations are important because fracture networks near an existing aquifer can become a geologic hazard during production. For this study, the combined use of seismic, seismic inversions, well logs, seismic attributes, mineralogy, and TOC one can detect brittle zones that can be targeted when hydraulic fracturing to enhance production and profitability of a shale gas play.

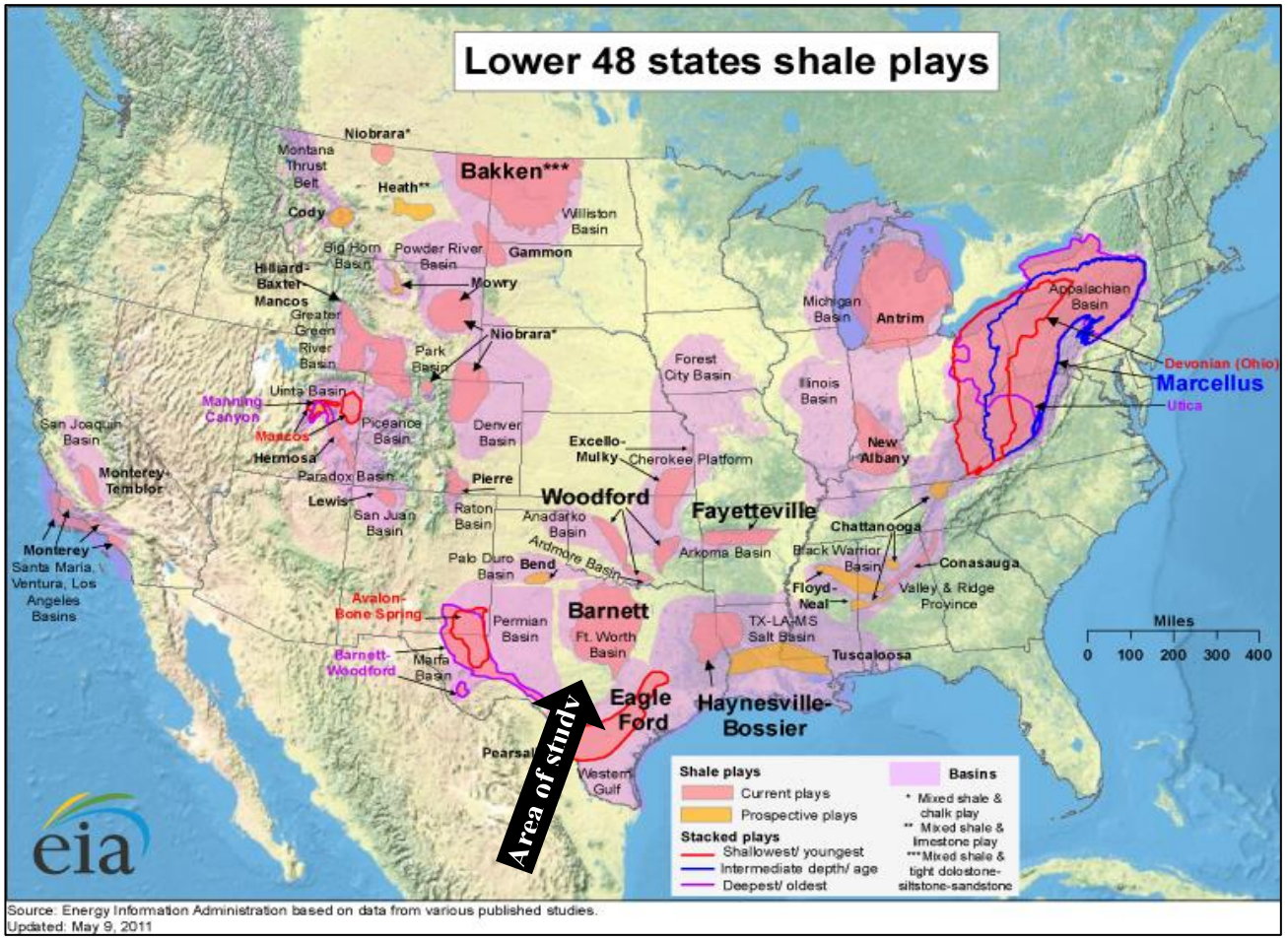

Figure 2. 1: Shale plays within the United States lower 48. Black arrow shows the area of study, Fort Worth Basin, for this project (EIA, 2011).

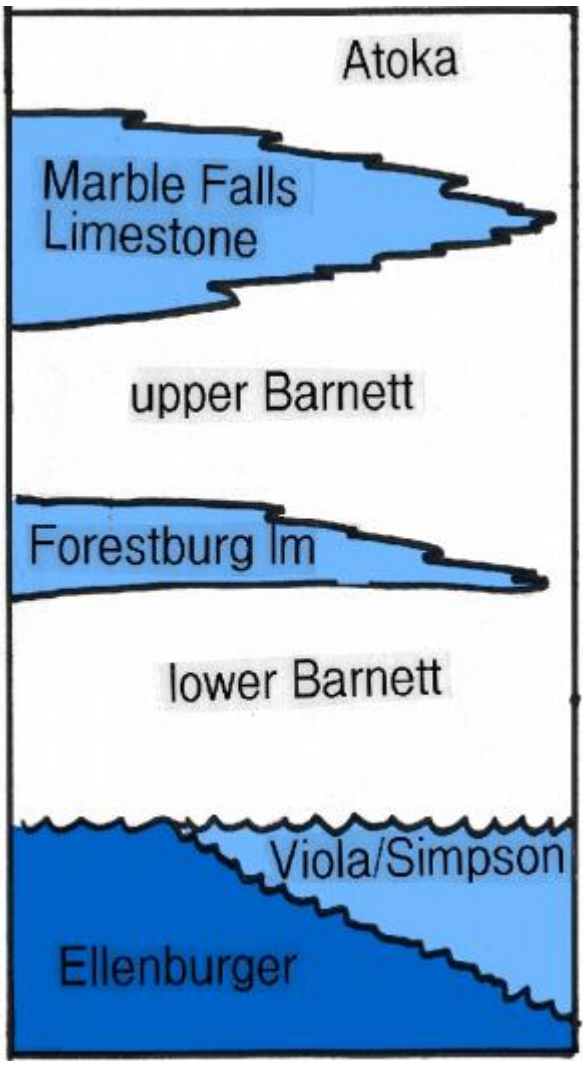

Figure 2. 2: Generalized stratigraphic column of the northerns portion of the Fort Worth Basin showing significant formations (Bowker, 2007).

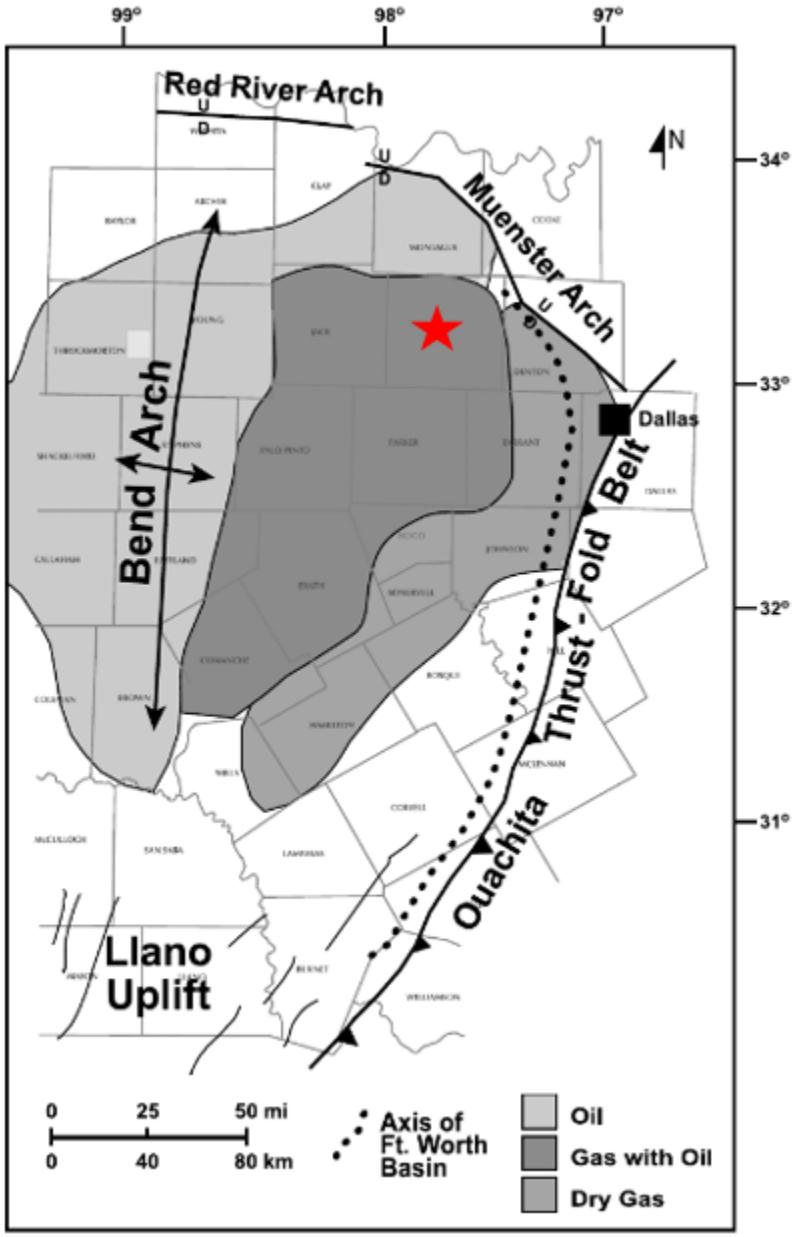

Figure 2. 3: Areal extent of the Barnett Shale within the Fort Worth Basin based on hydrocarbon production. The red star indicates the area of study (Montgomery et al., 2005).

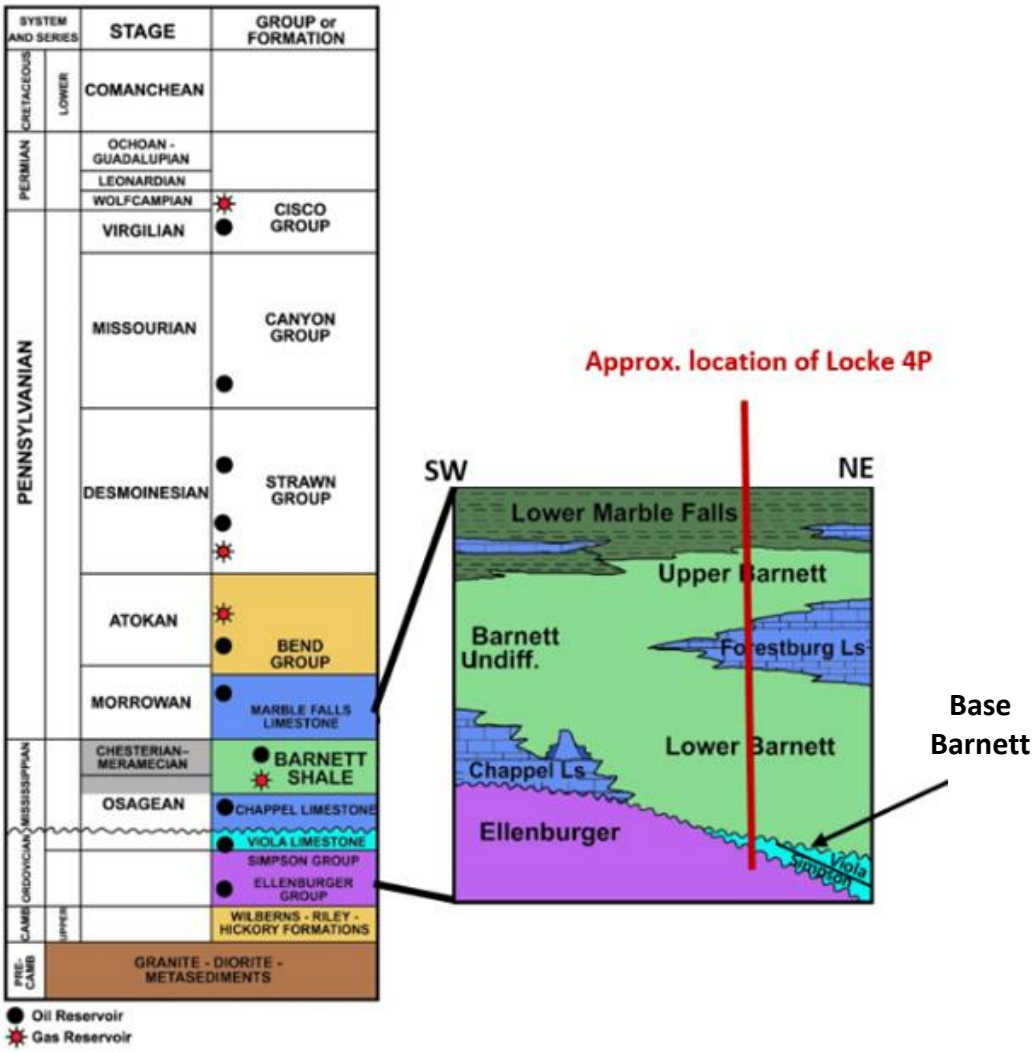

Figure 2. 4: Generalized stratigraphic column of the Fort Worth Basin and Barnett Shale with approximate well location used in this study (courtesy of Pioneer Natural Resources).

Chapter 3: Methods

Brittleness

A rock is considered to be brittle if when subjected to increasing stress, and exhibits little deformation before failing/breaking with little absorbed energy before failure. In contrast, if a rock is subject to increasing stress and undergoes large amounts of deformation before failing/breaking, with large amounts of absorbed energy before failure, the rock is considered to be ductile. Figure 3.1 shows a generalized diagram of the stages of deformation a rock undergoes when it is subjected to increasing stress. Elastic deformation is the first stage of deformation. Within the elastic deformation phase the applied stress deforms the rock; however, when the load is removed the rock returns to its original shape. Ductile is the next stage of deformation. When stress is applied to a rock the material deforms taking on a new shape; and when the stress is removed the rock remains deformed. The final stage of deformation is when the rock fails/fractures. When stress is continuously increased, the rock deforms until the rock breaks.

Brittleness is a function of, but not limited to, rock strength, lithology, texture, effective stress, temperature, fluid type (Handin and Hager, 1957; 1958; Handin et al., 1963; Davis and Reynold, 1996), diagenesis, and TOC (Wells, 2004). There is not one universal way to measure brittleness; however, with the combination of well log information and geomechanical properties, such as Young's modulus (E) and Poisson's ratio (υ), one can make estimates of a rock's brittleness. The importance of differentiating brittle from ductile zones is critical to hydraulic fracturing, where the goal is to develop a fracture network to increase the permeability within a zone of interest to allow the flow of hydrocarbons from the rock volume to the well bore to increase the oil and gas recovery.

I hypothesize that the Barnett Shale will be most brittle in areas with high quartz and TOC, while the more ductile areas will be more calcite rich and exhibit low TOC. This hypothesis is based on previous studies performed within the Barnett Shale by Perez and Marfurt (2013) and Bowker (2003a). This hypothesis was tested using both well logs and seismic data to calculate geomechanical properties and correlating those values to known values of pure minerals of quartz, calcite, and clay. Perez and Marfurt (2013) brittleness template calculated using mineralogy data from wells in a nearby location within the Barnett Shale (Figure 3.2), was used to test my hypothesis.

Seismic Interpretation

Eight formation tops were mapped using commercial software: Caddo, Marble Falls, Upper Barnett, Forestburg, Lower Barnett, Barnett Hard Shale, Base Barnett Unconformity, and the Ellenburger. Formation tops are used to perform the seismic prestack inversion to estimate brittle and ductile areas. Figure 3.3 shows the eight formation tops mapped in this study. The Ellenburger appears to be heavily karsted in the southwestern corner of the depth-structure map, confirmed by a horizon slice through the variance volume and vertical slices through the seismic amplitude volume (Figure 3.4). Karst collapse features that connect the Ellenburger aquifer to the Barnett Shale are known to be geologic drilling hazards and should be avoided to avoid water production from the underlying aquifer (Qi et al., 2014). Overall, the Barnett and Forestburg formations in this survey are relatively flat reflectors within the survey with little structure other than the karst collapse (Figure 3.4).

Brittleness Average

Grieser and Bray (2007) introduced a brittleness estimate using full wave sonic data to compute mechanical properties such as Young's modulus and Poisson's ratio. Young's measures the stiffness of a material (Figure 3.5) while Poisson's ratio measures the lateral expansion of a material divided by its axial compression (Figure 3.6). Grieser and Bray (2007) cross-plot Young's modulus versus Poisson's ratio and hypothesize that rocks with low Young's modulus and high Poisson's ratio are ductile, while rocks with high Young's modulus and low Poisson's ratio are more brittle. First they normalize Young's modulus:

$$E_{brittleness} = \frac{E - E_{min}}{E_{max} - E_{min}}, \qquad (3.1)$$

where E is Young's modulus and where E_{min} and E_{max} are the minimum and maximum values of Young's modulus measured from the well log data. Next, they normalize Poisson's ratio:

$$\upsilon_{brittleness} = \frac{\upsilon - \upsilon_{max}}{\upsilon_{min} - \upsilon_{max}}, \qquad (3.2)$$

where υ is Poisson's ratio and where υ_{min} and υ_{max} are the minimum and maximum values of Poisson's ratio measured from the well log data. Using $E_{brittleness}$ and $\upsilon_{brittleness}$ they define the brittleness average (BA) to be:

$$BA = \frac{E_{brittleness} + \upsilon_{brittleness}}{2}. \qquad (3.3)$$

Using the compressional (V_p) and shear (V_s) wave velocity well logs, Poisson's ratio and Young's modulus are (Mavko, 2009):

$$\upsilon = \frac{\left(\frac{V_p}{V_s}\right)^2 - 2}{\left\{2\left[\left(\frac{V_p}{V_s}\right)^2 - 1\right]\right\}}, \qquad (3.4)$$

and:

$$E = 2\rho V_s^{\,2}(1+\upsilon), \qquad (3.5)$$

where ρ is the density.

Following Perez (2013) following Wang and Gale (2009), the brittleness index (BI) was computed based on mineralogy:

$$BI_{Wang\ (2009)} = \frac{Qz+Dol}{Qz+Dol+Ca+Cly+TOC} \qquad (3.6)$$

where *Qz* is percent quartz, *Dol* is percent dolomite, *Ca* is percent limestone, *Cl* is percent clay, and *TOC* is percent total organic content. Perez (2013) calculated the brittleness index based on ECS log data. He then plotted gamma ray versus brittleness index for all the formations and divided the data into four equal brittleness types: brittle, less brittle, less ductile, and ductile zones. Perez (2013) observed that the brittle zones are due to higher quartz seen in the mid to lower part of the Lower Barnett. Interestingly, this more brittle area also contains greater amount of TOC, due to the depositional relationship between high quartz content in relation to high organic material preserved from radiolara and preserved in deeper less oxygenated water (Singh, 2008).

The results of the calculated geomechanical properties are shown and displayed in Figure 3.7. In general, the more ductile Forestburg limestone and underlying Base Barnett Unconformity (Perez's Viola formation) formations are considered to be fracture barriers for the locally more brittle Barnett Shale (Hill, 1992). Both the Forestburg and Base Barnett Unconformity lie in the more ductile regions of the Poisson's ratio and Young's modulus crossplot.

Total Organic Carbon (TOC) and its influence on Brittleness

TOC is the measure of the organic richness of a rock by measuring the organic carbon and kerogen content in a rock sample (Jarvie, 1991) and is vital component within the

Barnett Shale. TOC is measured in weight percent and is good measurement of the hydrocarbon potential of a source rock. Based on Wang et al's. (2009) equation 3.6, as TOC increases the brittleness index (BI) of a rock sample decreases. However, Bowker (2003a) and Perez (2013) found that quartz rich zones within the Barnett Shale are correlated to high TOC and are more brittle and productive with the effect of increased kerogen not compensated by a greater increase in quartz. In contrast, the more ductile intervals in the Barnett Shale have low TOC with high clay and calcite content.

No cuttings or core were given for this study so TOC was modeled using Passey's equation (3.7):

$$TOC = (\Delta LogR) * 10^{2.297-0.1688*LOM}, \qquad (3.7)$$

where LOM is the Level of Organic Metamorphism that relates to thermal maturity and where

$$\Delta LogR = log_{10}\left[\left(\frac{Res}{Res_{base\ line}}\right) + 0.02 * (\Delta t - \Delta t_{base\ line})\right]. \quad (3.8)$$

In these equations $Res_{base\ line}$ and $\Delta t_{base\ line}$ represent the deep resistivity and the sonic baseline measured in a non-source rock. The results of this calculation are shown as track 9 of Figure 3.7. The modeled TOC results were compared to Perez (2013) TOC measurements for validation. I anticipate the high TOC regions to occur in the more brittle zones due to corresponding high quartz content.

λρ and μρ

$\lambda\rho$-$\mu\rho$ are seismic measurements of the Lame parameters incompressibility (λ) and rigidity (μ). For good quality seismic gathers one can estimate P-impedance, Z_p, and S-impedance, Z_s. For very high quality long offset data one can also estimate density, ρ. In the absence of such long offset data:

$$\lambda\rho = (\rho V_p)^2 - 2(\rho V_s)^2 = {Z_p}^2 - {Z_s}^2 \quad (3.9)$$

$$\mu\rho = (\rho V_s)^2 = {Z_s}^2 \quad (3.10)$$

where Z_p is P-impedance (ρV_p) and Z_s is S-impedance (ρV_s), ρ is the the density and V_p and V_s are the compressional and shear wave velocities. Goodway et al. (1997) found that $\lambda\rho$-$\mu\rho$ crossplots from seismic and well log data can reveal information about lithology and pore fluid.

Mavko et al. (2009) published moduli, density, and velocities for common minerals, including the primary minerals that comprise the Barnett Shale including: quartz, calcite, and clay (Table 3.1). Using Mavko et al.'s (2009) values for these three minerals, Perez and Marfurt (2013) generated a mineralogy ternary diagram in $\lambda\rho$-$\mu\rho$ space from well and seismic data. I will use Perez and Marfurt's (2013) template and color bar to distinguish brittle and ductile zones.

Prestack Seismic Inversion

The objective of prestack seismic inversion is to obtain estimates of P-wave impedance, S-wave impedance (and density if far offsets are available) which can then be used to predict fluid and lithology properties.

Wavelets are extracted from angle-limited stacks using Fatti's et al.'s (1994) approximation to the Zoeppritz equations:

$$R(\Theta) \approx \frac{\Delta Z_p}{2Z_p}\left(1 + tan^2(\Theta)\right) - 8[\frac{Z_s}{Z_p}]^2 \frac{\Delta Z_s}{Z_s} sin^2(\Theta), \quad (3.11)$$

where Z_p is the background model P-impedance, Z_s is the background model S-impedance, ΔZ_p is the vertical change in P-impedance, ΔZ_s is the vertical change in S-impedance, and Θ is the angle of incidence. Using equation 3.11, the angle-limited stacks can be inverted to obtain P-impedance and S-impedance (Verma, 2015).

With the combination of seismic data, P-wave sonic, S-wave sonic, and density from well log information one can invert seismic prestack data to obtain estimates of P and S impedance. Wavelets were extracted using the well that had an average phase of -51 degrees (Figure 3.8) therefore, a +51 degrees phase shift was applied to the seismic to phase match the data. Next, Well 4P was tied to the seismic data using the previously mapped formation tops to the synthetic prestack response (Figure 3.9). Following the standard workflow for the commercial software (Hampson and Russell 2005; Russell et al., 2006) wavelets were extracted for 0-10, 11-20, and 21-30 degrees angle-limited stacks (Figure 3.10). Farther offsets were not used because of misalignments with far offset traces due to data conditioning and anisotropy effects of the Marble Falls formation discussed briefly in the appendix which may be investigated further in another study. Figure 3.11 shows the correlation and error between the modeled gathers and the measured gathers. There was a high correlation of 91.2% with an error of 41.1%. The error does not appear to be geological so it was interpreted as random noise.

Using Fatti's equation, equation 3.11, the three angle limited stacks were simultaneously inverted to obtain P and S impedances (Figure 3.12). Figure 3.13 shows an additional inversion analysis in a crossline orientation. Next, the relative error was calculated using:

$$Relative\ Error = \frac{|angle\ gather - synthetic\ angle\ gather|}{rms(angle\ gather)}, \qquad (3.12)$$

where rms is the root mean square of the amplitude of the gathers. Dividing by the rms results gives a relative error that is independent from amplitude variations between traces. The median of the relative error between the top of the Upper Barnett to the top of the Ellenburger was computed using a commercial software workflow (Figure 3.14). The error is low with a median error of ~0.025 (2.5%) with a maximum error of 6%.

Using the calculated P-impedance and S-impedance from the prestack inversion $\lambda\rho$ and $\mu\rho$ were computed using equations 3.7 and 3.8. Just like in the case of the well log $\lambda\rho$-$\mu\rho$ crossplots, mineral ternary plot was created in the $\lambda\rho$-$\mu\rho$ space using a color bar (Figure 3.15).

Microseismic Data

Microseismic events are known to be indicators of fractured or damaged rock volumes that have been brought to failure due to high stresses such as those induced by hydraulic fracturing (Cai et al., 2011). The imaging and interpretation of microseismic events provides interpreters insight about the fracture network within the reservoir (Maxwell et al., 2010).

Hydraulic fracturing is the process of injecting fluid at high pressures through perforated holes, typically water with additives to make it slippery and to suppress corrosion, as well as sand or ceramic grains to prop open any induced fractures. The objective is to create or open existing fractures within a rock to allow the flow of hydrocarbons in the rock, up and through the well bore, and to the well head. When stress is applied to a brittle rock the rock fails/fractures. So long as the pressure is not increased further, the more ductile/plastic rocks act as a seal. Injected fluid decreases the effective stress in the rock shifting the Mohr circle to the left (Figure 3.16) towards the failure curve.

In most cases, when a rock fails a microseismic event occurs. Because brittle rocks fail easier than ductile rocks, microseismic events are good indicators of brittle zones, allowing them to calibrate surface seismic data inversion-based brittleness estimations.

In general, more brittle rocks contain more microseismic events than ductile rock zones. Plotting the microseismic events alongside the seismic data the events were used as a

validation for the brittleness estimates, estimated using $\lambda\rho$ and $\mu\rho$. Microseismic events were recorded for each of the thirteen hydraulic fracturing stages.

Fracture Detection Using Borehole Image Logs

Borehole imaging uses a variety of methods to obtain an image of the borehole wall based on some property contrast. One of the more common methods is recording changes in micro-resistivity along the borehole, allowing the interpreter to map fracture locations and orientations. Image logs are acquired by applying an electrical current to the borehole wall and then measuring its resistivity (Cook, 2016). The borehole image provides information about the borehole geometry which can be used to interpret breakouts, natural fractures, induced fractures, and the stress field (Tingay et al., 2008). Fractures are interpreted as either resistive or conductive. Resistive fractures are interpreted to be mineralized and impermeable while conductive fractures are interpreted to be open and permeable to fluid flow (Stearns, 2015).

Borehole images are acquired and interpreted for the horizontal section of well 2H courtesy of Baker Hughes. Image logs provide information about the fractures on the borehole wall. In this survey, the image logs will identify any zones of weakness that may be reactivated by the microseismic data. Understanding the relationship between fracture type and microseismic event activity within a formation can result in better well planning to reduce cost when hydraulically fracturing an unconventional shale play.

Curvature Attribute

Structural curvature is a seismic attribute computed by using the inline and crossline dips calculated from the seismic amplitude data (Chopra and Marfurt, 2008). Structural curvature measures strain which can often be correlated with natural fractures (Staples,

2011). Figure 3.17 shows a schematic 2D section of a curved surface showing anticlinal and synclinal structures as seen in outcrops. Previous studies by Staples (2011) found a correlation between fracture intensity and curvature based on a plate bending analysis, with fractures most likely to occur in areas with the highest amounts of strain. For this reason, one can hypothesize that there may be more natural fractures along the very concave and convex portions of synclinal and anticlinal structures.

Brittleness Classification Volume

Using commercial software I created a brittleness classification horizon probe between the top of the Forestburg limestone and the top of the Base Barnett Unconformity formations using $\lambda\rho$ and $\mu\rho$ volumes as an input. Using the brittleness template from Perez and Marfurt (2013); brittle, less brittle, less ductile, and ductile regions were classified for the horizon probe. The horizon probe was converted into a seismic volume the brittleness classification was extracted at every microseismic event location to test the hypothesis that events correspond to brittle and less brittle zones.

Study Limitations

Only one pilot well with well logs was available and one deviated well with microseismic events was available within the seismic study area. The limited amount of well data creates a significant amount of uncertainty when attempting to validate the results. Another limitation is when solving for brittleness average it is only a function of compressional and shear velocities as well as densities and does not take into consideration mineral composition and percentages. However, using the brittleness template based on the calculated brittleness index log based on the ECS log from Perez (2013) I was able to reduce some of the uncertainty. When computing $\lambda\rho$-$\mu\rho$ for quartz,

clay, and calcite by Mavko et al. (2009) the mineral ternary diagram used for this study assumed a porosity of zero percent which ignores the contribution of natural fractures and pores.

No core data are available for this study which therefore lacks direct laboratory measurements of geomechanical properties. Log measurements were used to estimate geomechanical properties which can result in some amount of uncertainty. Well log measurements themselves are prone to some error. According to Perez (2013) ECS only measures elemental abundances and relies on rules to reconstruct mineral assemblies, and is not able to differentiate between different mineral forms that can exhibit different geomechanical strengths that affect the geomechanical properties of the rock itself.

Lastly, borehole images only image the borehole wall and the surrounding area of the borehole is unknown. With the lack of real rock data the images cannot be directly validated (Donselaar and Smith, 2005).

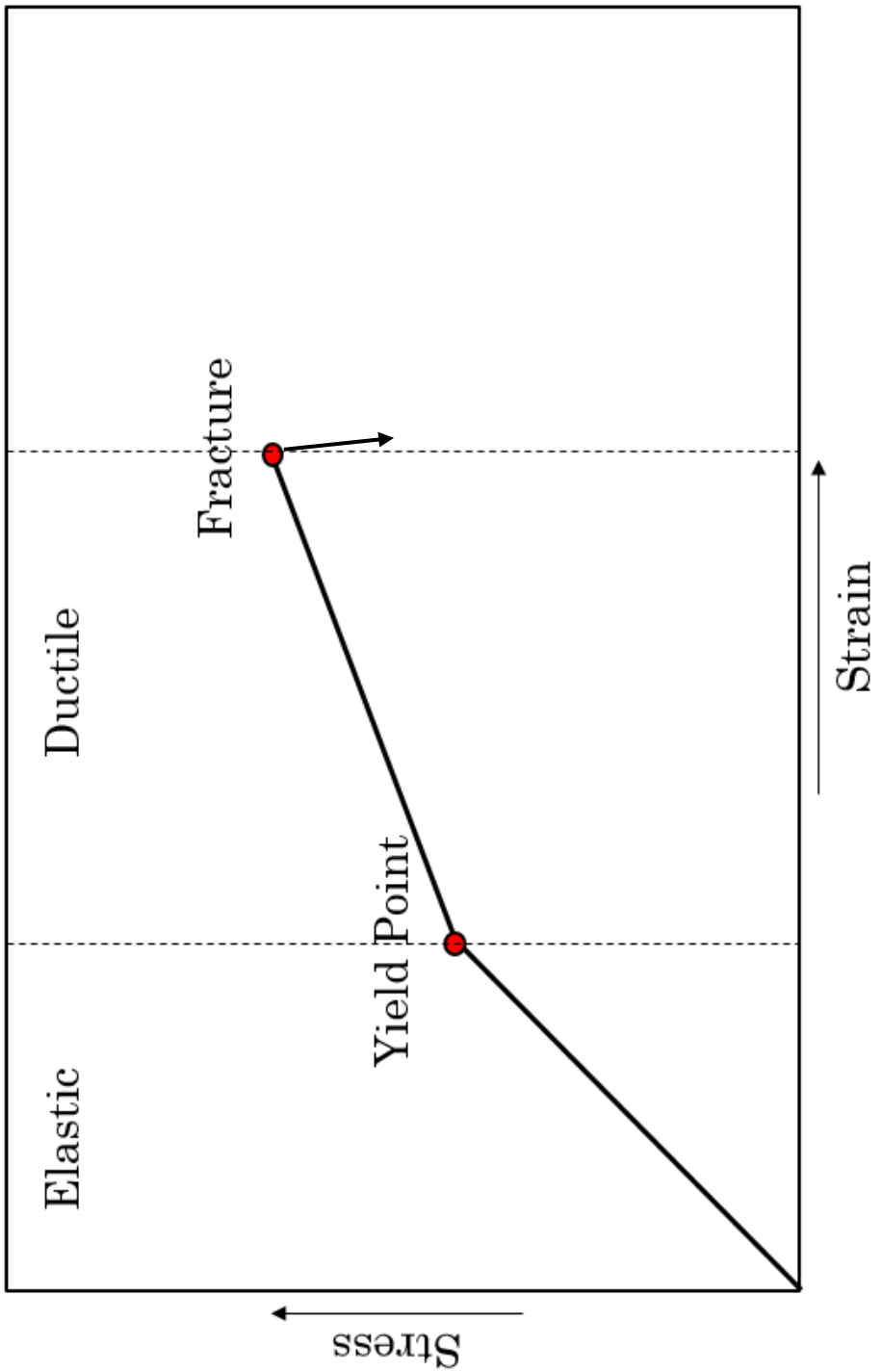

Figure 3. 1: Stages of deformation with increasing stress.

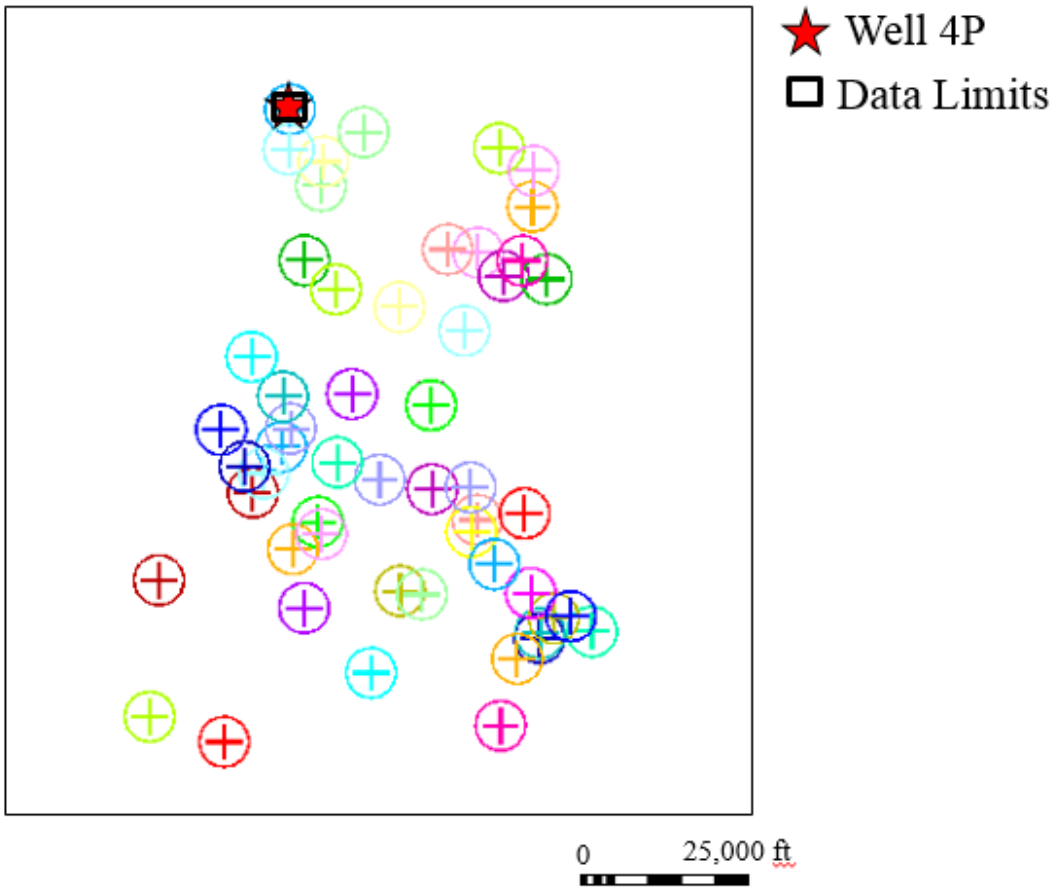

Figure 3. 2: Map view showing well 4P used in this study relative to Perez and Marfurt (2013) study wells.

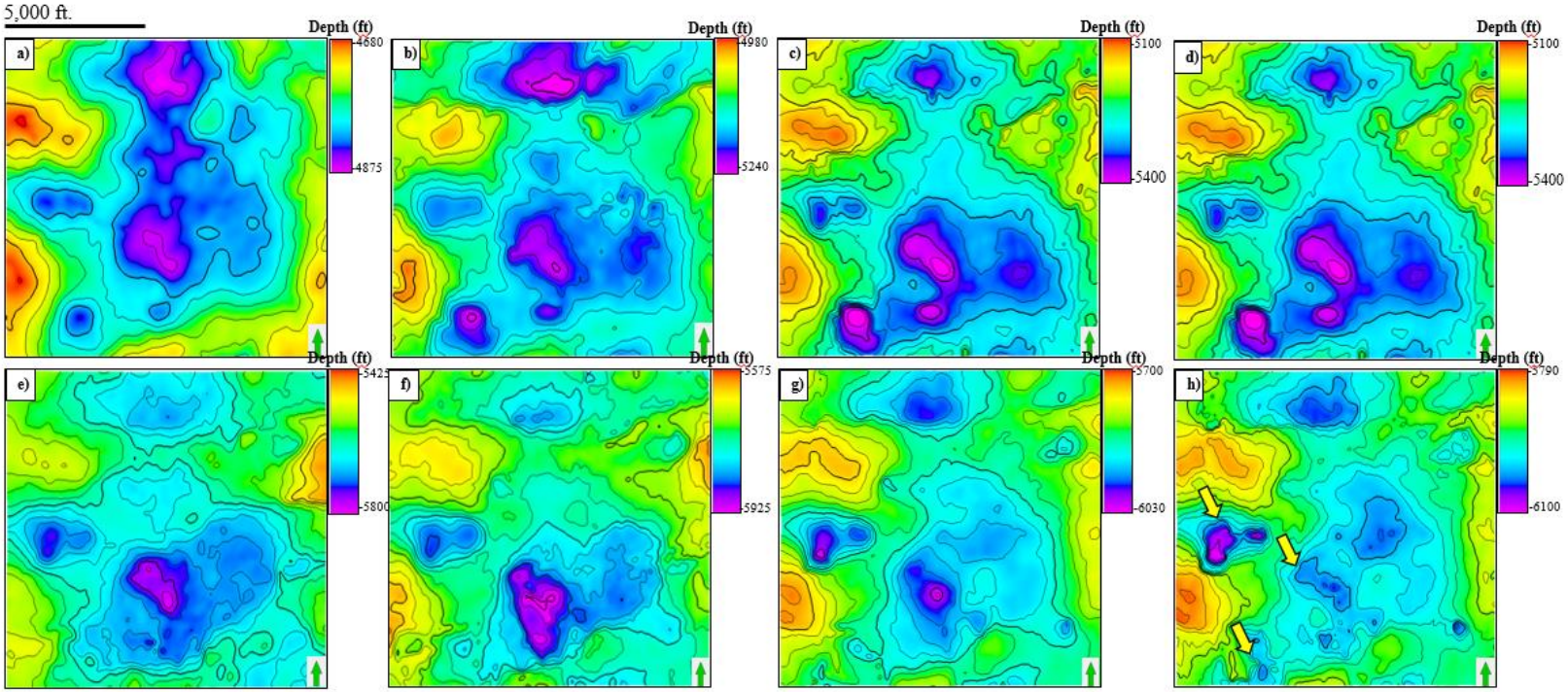

Figure 3. 3: Depth structure maps of the top (a) Caddo, (b) Marble Falls, (c) Barnett, (d) Forestburg, (e) Lower Barnett, (f) Barnett Hardshale, (g) Base Barnett Unconformity, (h) Ellenburger formations. Yellow arrows indicate karst collapse features in the Ellenburger.

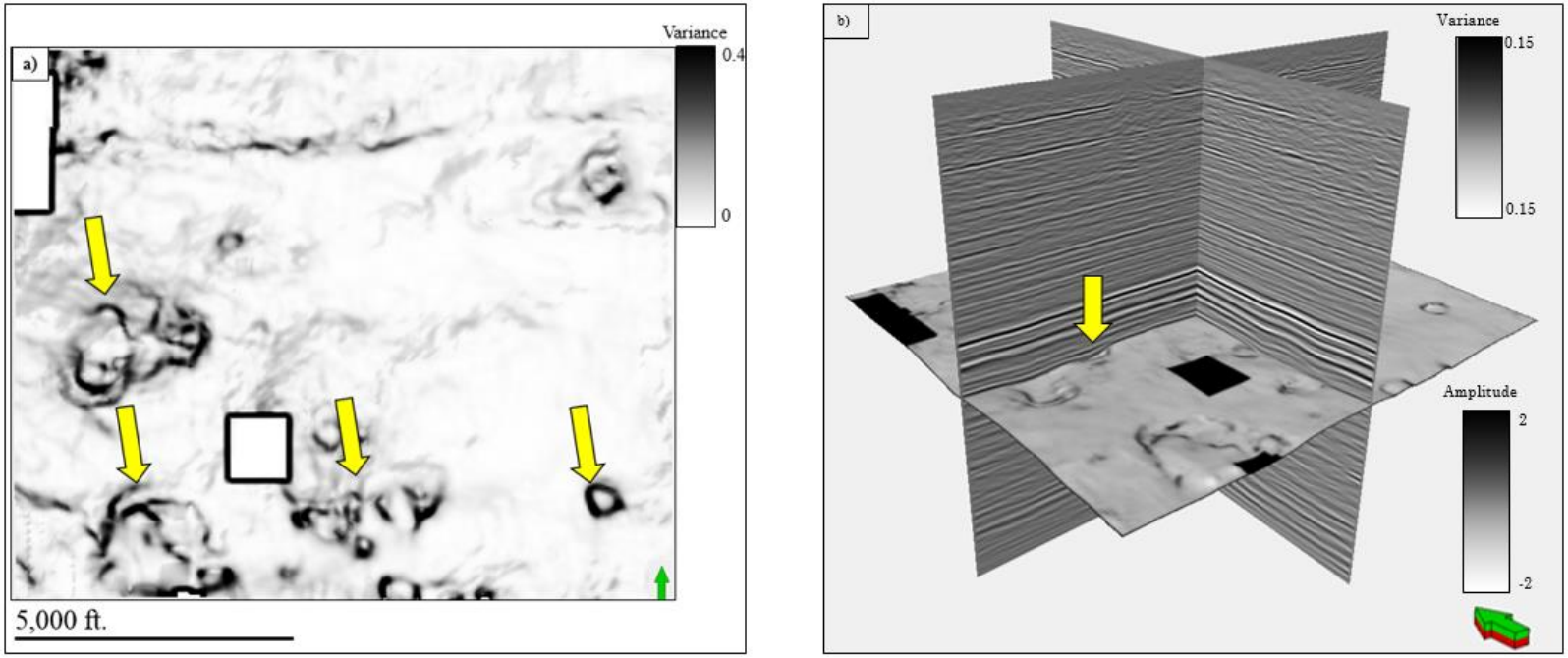

Figure 3. 4: (a) Variance attribute extracted along the top Ellenburger horizon slice. (b) Variance horizon slice with amplitude in the vertical section. Yellow arrow indicates the karst collapse feature corresponding to a bowl like shape in the amplitude section and the edge shown by the variance.

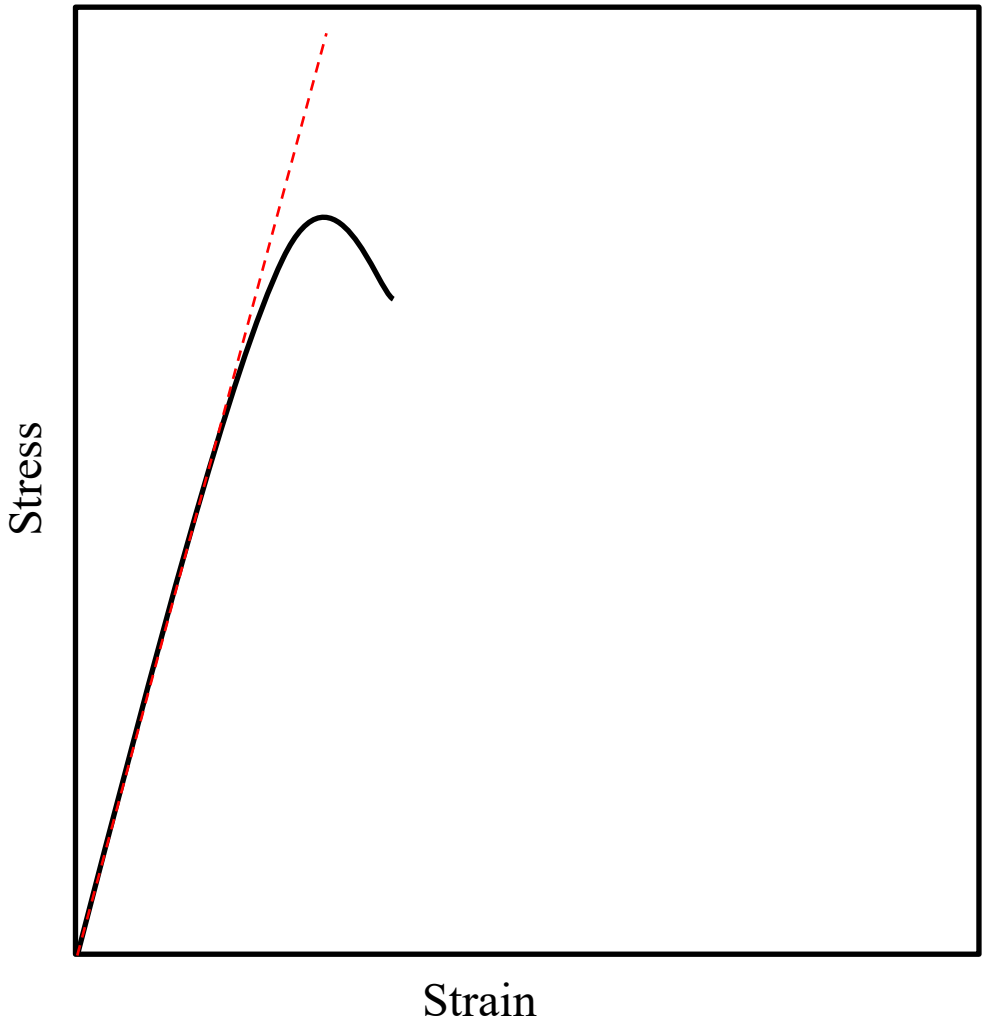

Figure 3. 5: Stress-strain diagram of a rock volume subjected to increasing stress, the slope of the linear portion of the line intersecting the origin is Young's Modulus. The steeper the slope the larger Young's

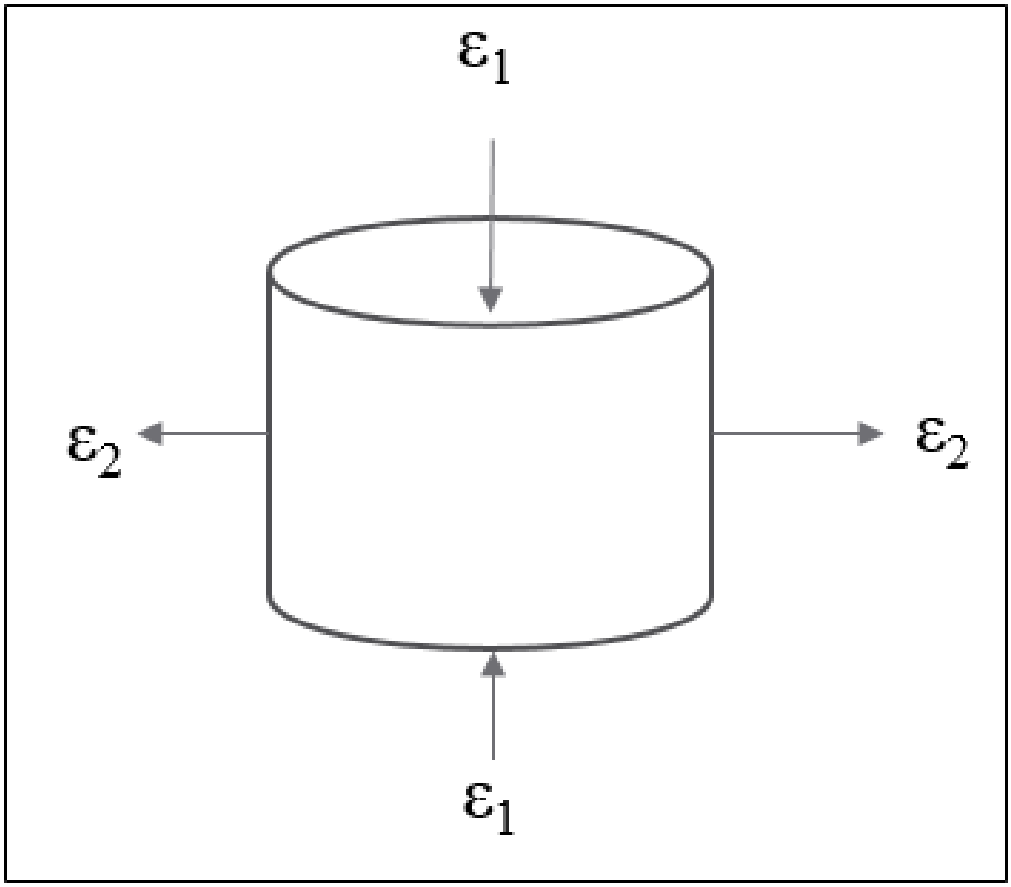

Figure 3. 6: Poisson's ratio is the measurement of the expansion of a material divided by the axial compression ($\varepsilon_1/\varepsilon_2$). The larger the Poisson's ratio, the more brittle a material. The average Poisson's ratio for the three main minerals in the Barnett are given by: Quartz= 0.064, Clay= 0.14, Calcite= 0.3.

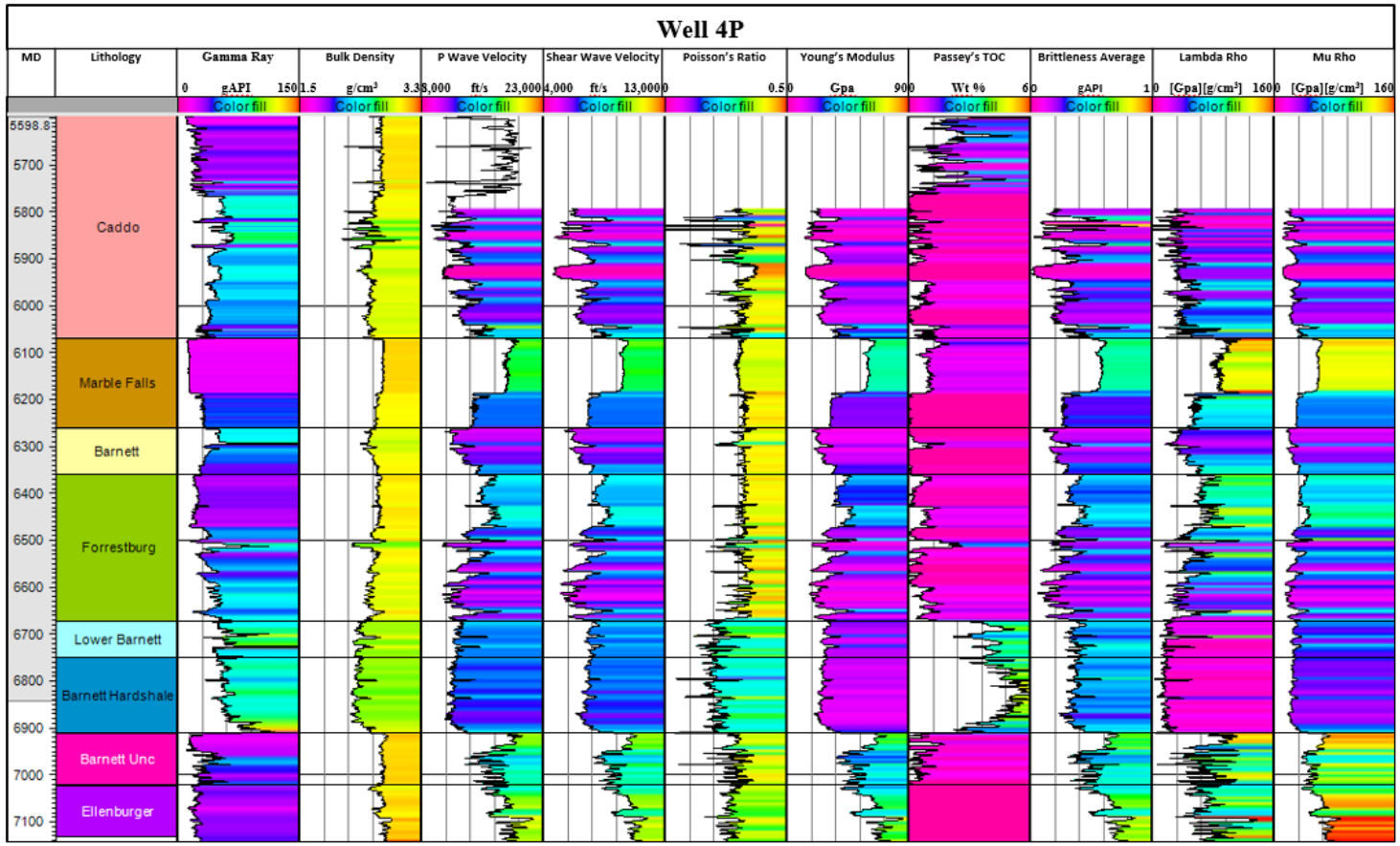

Figure 3. 7: Calculated geomechanical properties from well logs. Track 7 and 8, Poisson's ratio and Young's modulus, are crossploted against each in Figures 5.1, 5.2, and 5.3. Track 9 is TOC calculated using Passey's equation.

Mineral	Quartz	Clay	Calcite
$\lambda\rho$ (GPa)(g/cm^3)	20.32	48.45	149.41
$\mu\rho$ (GPa)(g/cm^3)	116.60	22.95	88.08
Young's Modulus (E)	95.756	3.203	84.293
Poisson's Ratio (υ)	0.064	0.144	0.317

Table 3. 1: $\lambda\rho$, $\mu\rho$, Young's Modulus, and Poisson's Ratio values for the three most common pure minerals within the Barnett Shale by (Mavko, et al., 2009).

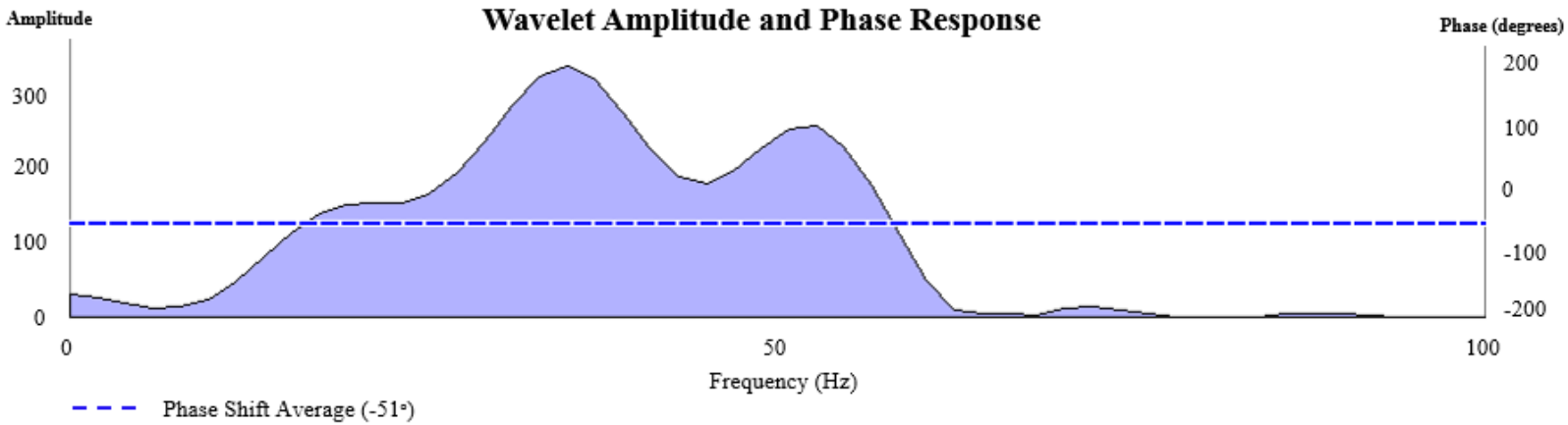

Figure 3. 8: Average phase of the prestack seismic data used for the seismic inversion.

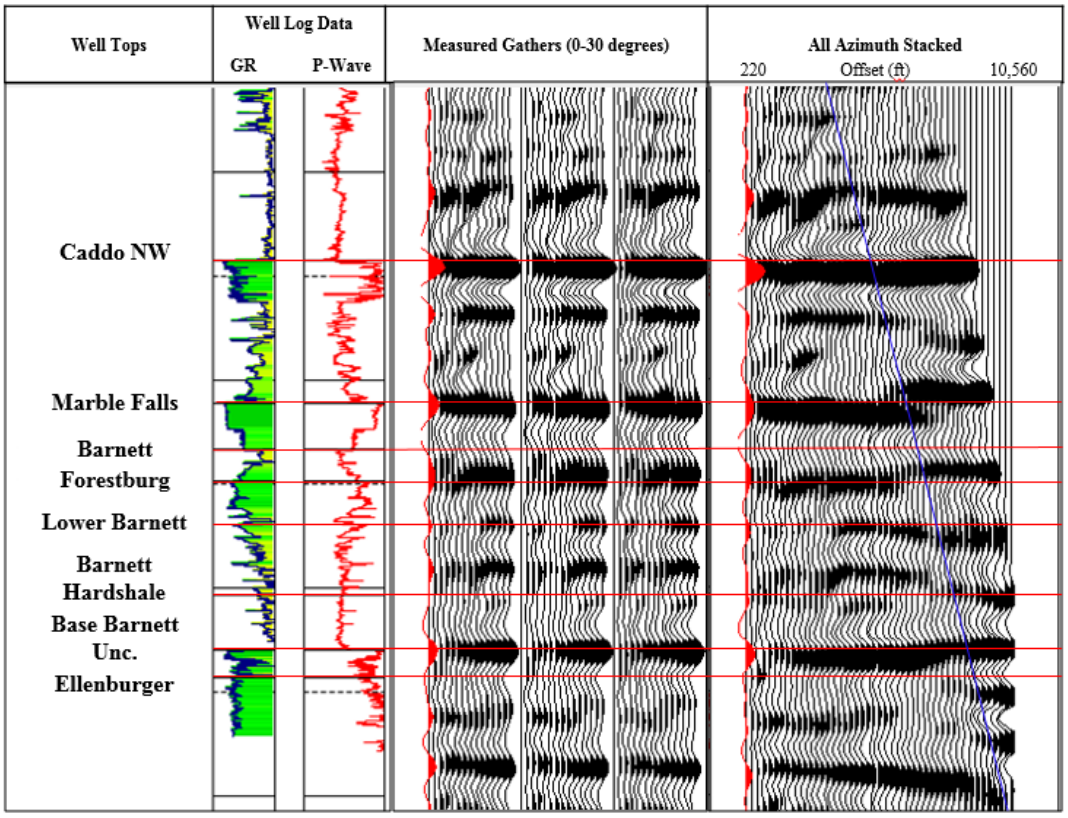

Figure 3. 9: Seismic data to well tie. The red horizontal lines are the formation tops used to compute the well-tie using the measured gathers. To the left of the blue line are the offsets that were considered for this study and to the right are offsets that were muted (>30 degrees) (discussed in Appendix A).

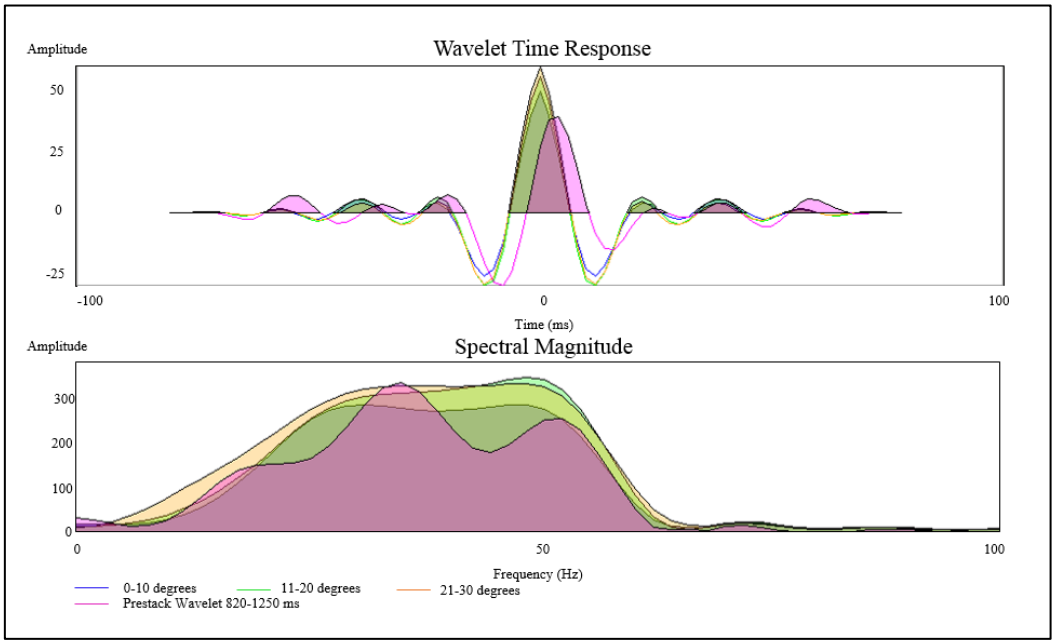

Figure 3. 10: Wavelet extracted from the 4P well for the angle limited stacks. The wavelets are extracted for angles 0-10, 11-20, 21-30, and all angles combined with amplitude ranges from -25 to 50.

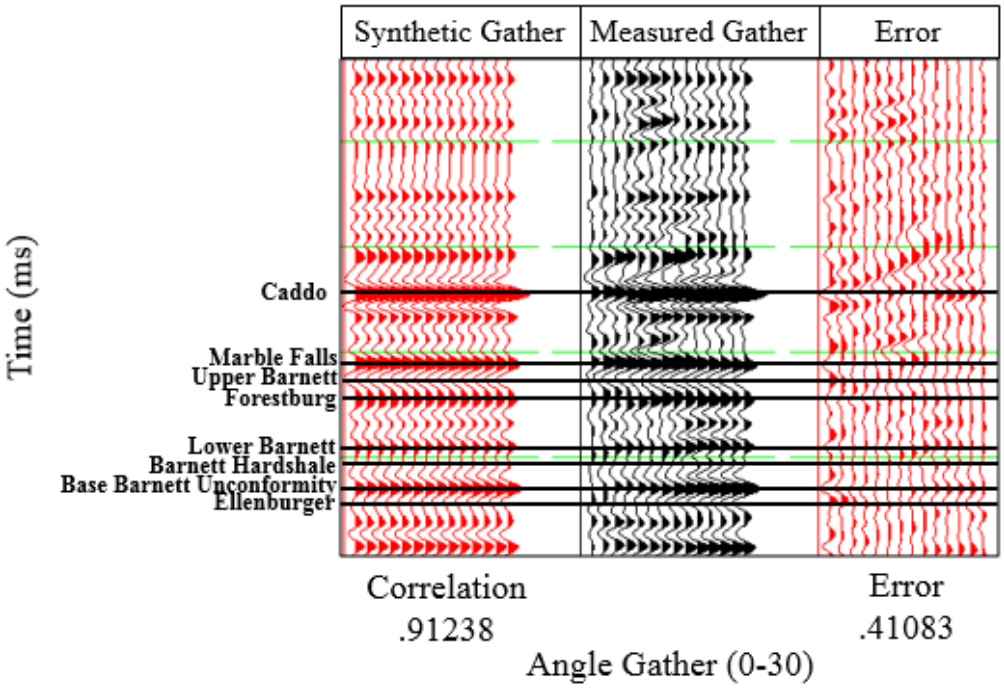

Figure 3. 11: Misfit between the modeled and measured gathers. The error is the difference between the two.

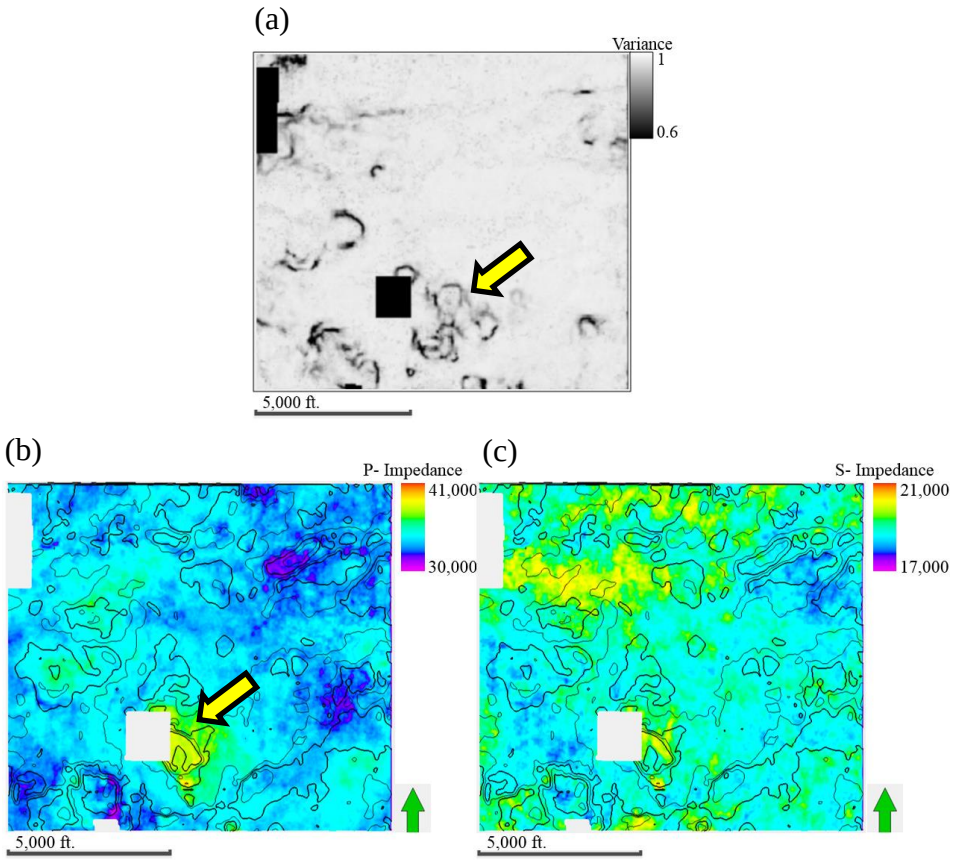

Figure 3. 12: (a) Variance extracted along the Base Barnett Unconformity formation. Yellow arrow indicates a karst collapse feature, (b) Calculated average P impedance from the top of the Barnett to the top of the Base Barnett Unconformity formation. Yellow arrow indicates a high anomalous impedance in a karst collapse feature, (c) Calculated average S impedance from the top of the Barnett to the top of the Base Barnett Unconformity formation.

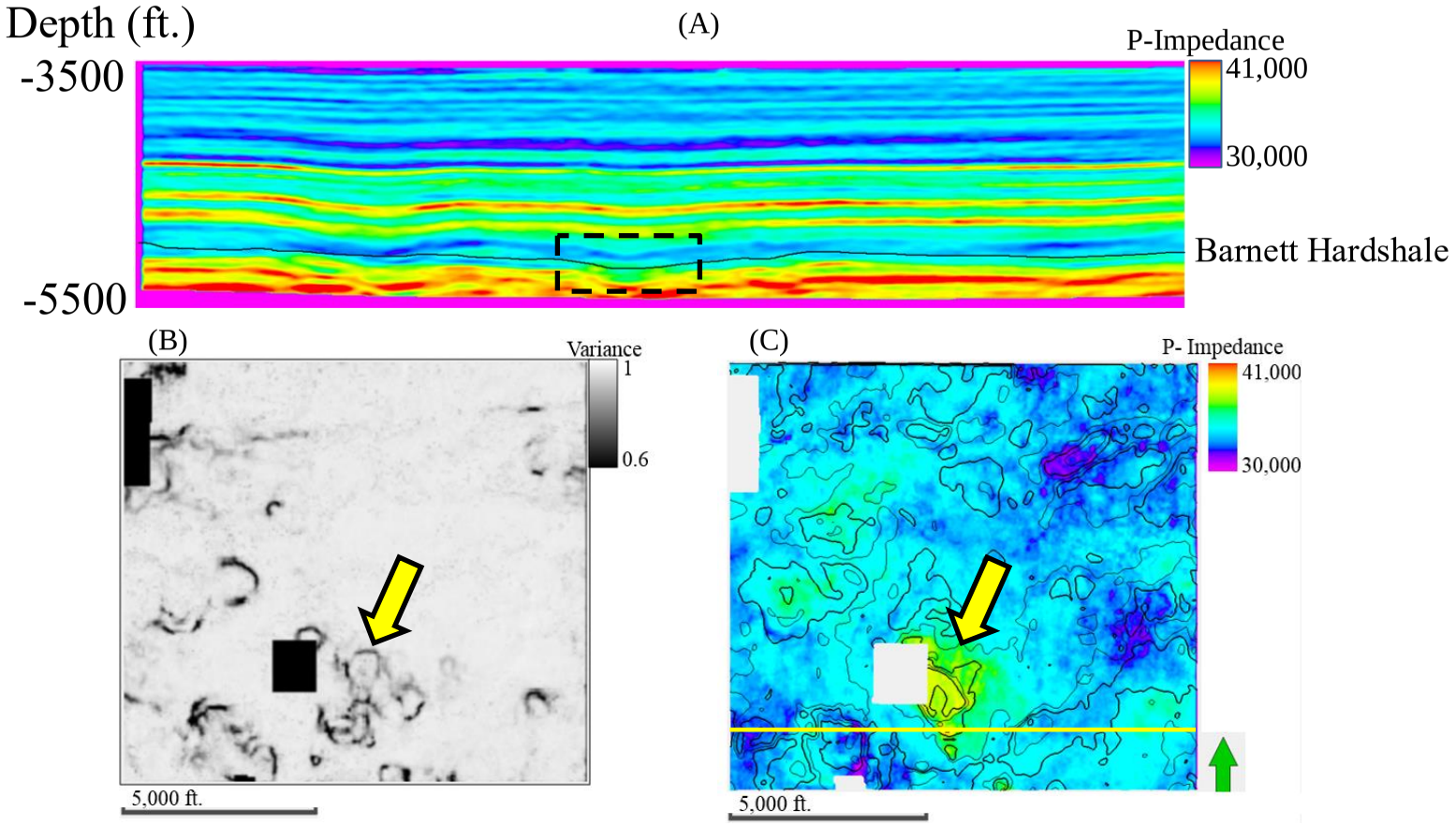

Figure 3. 13: (A) Crossline section through the anomalous P-impedance area. Black box indicates an increase in P-impedance where karst collapse feature is located. This anomaly is due to thicker bedforms containing increased biogenic quartz content resulting in a decrease in porosity, therefor an increase in density, resulting in an increase in P-impedance. (B) Variance extracted along the Base Barnett Unconformity, (C) Average P-impedance of the Barnett shale

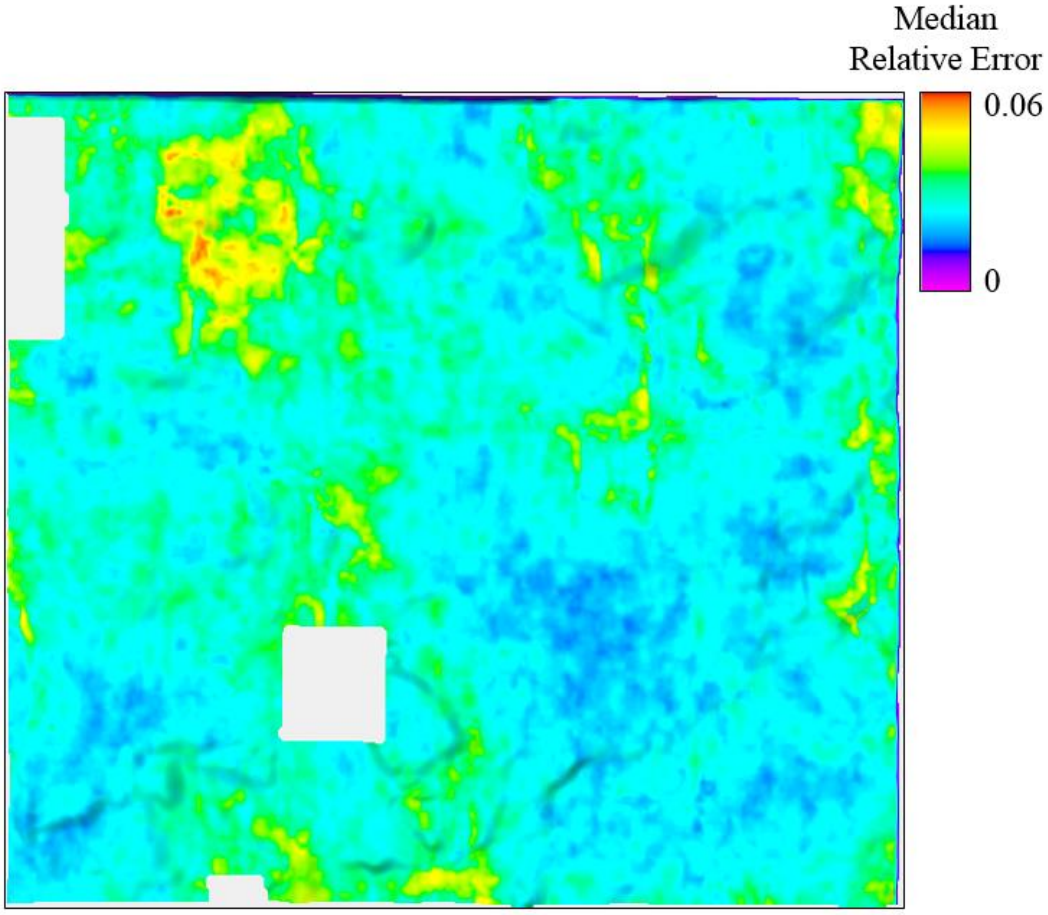

Figure 3. 14: Median relative error from the prestack data inversion from the top of the Upper Barnett to the top of the Base Barnett Unconformity.

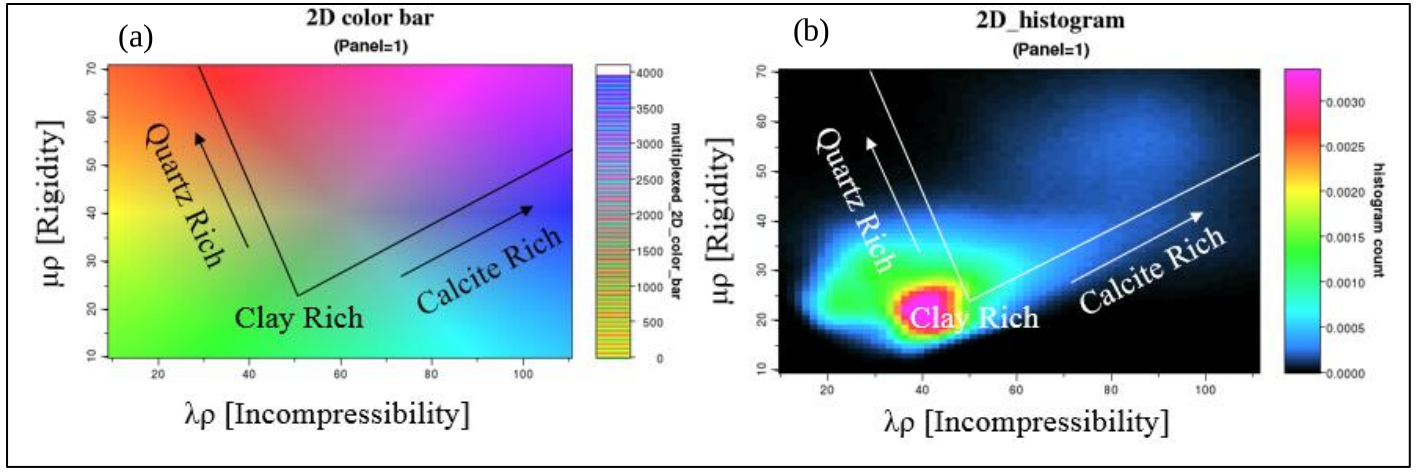

Figure 3. 15: (a) 2D colorbar with mineral ternary diagram lying in the λρ and μρ space, (b) 2D data histogram with mineral ternary diagram in the λρ and μρ space. Colorbar is clipped to fit data shown by the 2D histogram.

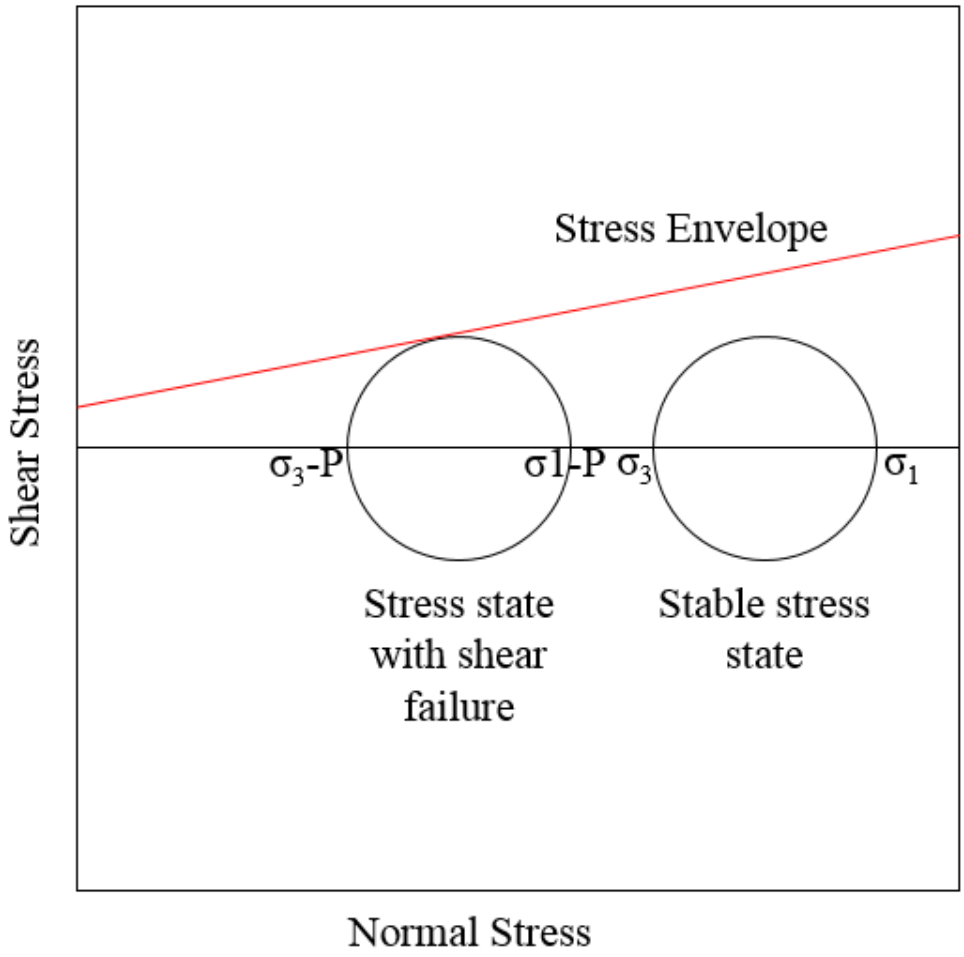

Figure 3. 16: Mohr circle diagram. Mohr circle shifts left when fluid injected. σ_1 is the maximum effective stress and σ_3 is the minimum effective stress, and P is the pressure of the fluid.

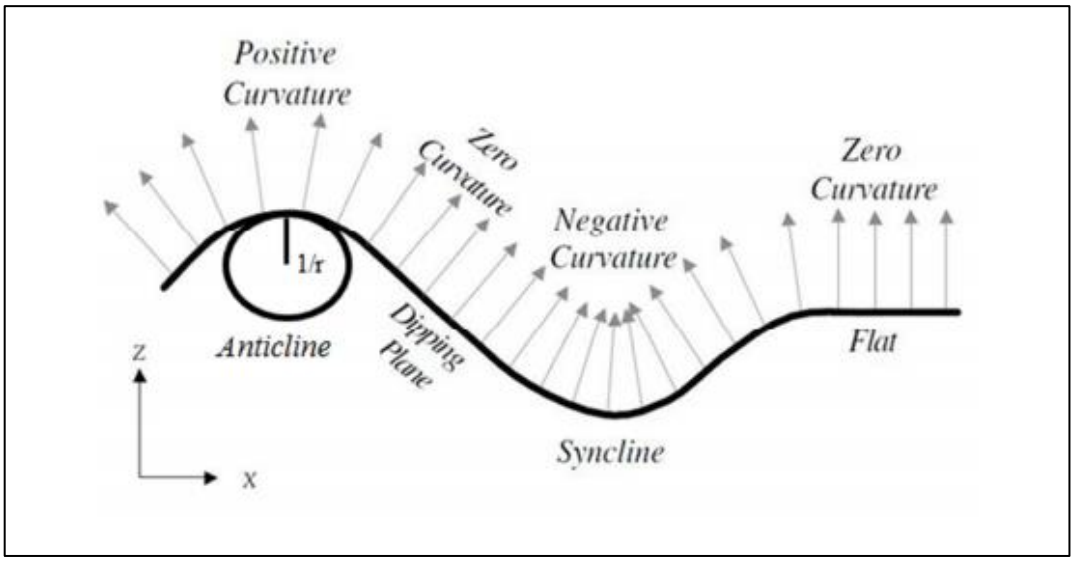

Figure 3. 17: Schematic 2D section of a curved surface featuring anticlinal and synclinal structures. Positive curvature is defined as anticlinal features while negative curvature is defined as synclinal features. The curvature (*k*) is defined by 1/*r*, where *r* is the radius of the circle that is tangent and fits to each point of the curve (Roberts, 2001).

Chapter 4: Results

Young's Modulus and Poisson's Ratio Cross Plots

Crossplotting Poisson's ratio versus Young's modulus shows relationship between the two moduli (Figure 4.1a). Limestone formations exhibit a moderate to high Young's modulus with a high Poisson's ratio while shale formations exhibit a moderate Young's modulus values with a low Poisson's ratio with the exception of the Upper Barnett. Overlaying Perez and Marfurt's (2013) brittleness template and overlaying it on the Young's modulus versus Poisson's ratio in Figure 4.1b shows that the limestone formations (Caddo, Marble Falls, and Forestburg) fall in the more ductile zones of the template while the Lower Barnett lies in the more brittle zones. The Upper Barnett is more ductile compared to the Lower Barnett sections due to a higher carbonate content. Karastathis (2007) found using FTIR, that the most abundant carbonate minerals within the Upper Barnett was calcite, dolomite, siderite, and aragonite.

TOC and Brittleness Affects

Wang and Gale (2007) show that total organic carbon (TOC) should increase brittleness. In the case of the Barnett Shale the more brittle zones have high TOC, due to the association of TOC with biogenic quartz. Using Passey's equation, TOC was modeled and plotted in color against $\lambda\rho$ versus $\mu\rho$ in Figure 4.2. High TOC corresponds with more brittle formations like the Barnett Shale, while low TOC corresponds with more ductile formations like the Forestburg, Marble Falls, and Base Barnett Unconformity.

λρ-μρ Crossplots

Using the calculated Lame parameters from Figure 3.7 to create a λρ-μρ crossplot, Perez and Marfurt's (2013) brittleness template was overlayed on the λρ-μρ space

(Figure 4.3). The Lower Barnett and the Barnett Hardshale are the most brittle portions of the Barnett, while the carbonate Forestburg, Base Barnett Unconformity, and the Marble Falls (formations that bound the Barnett) lie within the ductile regions. Overlaying the mineral ternary diagram for quartz, clay, and calcite, based on Mavko et al. (2009) the more ductile zones are rich in calcite while the more brittle zones are rich in quartz and clay content and low in calcite. In contrast, Grieser and Bray's (2007) brittleness average displayed in Figure 3.7, shows the Upper Barnett, Forestburg, Lower Barnett, and Barnett Hardshale, to be ductile and the Marble Falls and Base Barnett Unconformity to be brittle. This prediction is counter to Hill's (1992) observation and inconsistent with microseismic event location. Greiser and Bray's (2007) is an empirical relationship between Poisson's ratio and Young's modulus does not consider mineralogy or other geologic factors that may affect brittleness. Therefore, these results are not reliable when determining brittleness zones.

λρ and μρ from Seismic Prestack Inversion

From the prestack inversion P and S impedance estimates were used to predict the geomechanical behavior of the Barnett Shale. A vertical slice of $\lambda\rho$ and $\mu\rho$ of the seismic volume is shown in Figure 4.4 A and B. The limestone formations (Caddo, Marble Falls, Forestburg, Base Barnett Unconformity, and Ellenburger) exhibit higher λρ and μρ values compared than the Barnett shale formations. A gamma ray log is shown with the vertical section of the λρ and μρ seismic volumes. Low gamma ray values indicate limestone formations while high gamma ray values are indicative of the more radioactive Barnett Shale formations.

Figure 4.5 A shows a $\lambda\rho$-$\mu\rho$ crossplot using a 2D color bar. These values are then used to color the seismic volume which can then be correlated to lithology based on the examination of the ternary diagram. 2D histogram from Figure 4.5 (B) clipped $\lambda\rho$ to range between10-70 [GPa][g/cm^3] and $\mu\rho$ to range between 10-40 [GPa][g/cm^3] to better span the spectrum. Limestone formations: Marble Falls, Forestburg, and Base Barnett Unconformity are represented by purple, magenta, and blue colors which correspond to calcite rich formation. The Barnett Shale is dominated by green, yellow, and red colors which correspond to clay and quartz rich formations. Comparatively, the Lower Barnett is more quartz rich compared to the more clay rich Upper Barnett (Figure 4.6).

Validating Brittleness Estimations with Microseismic

Microseismic events correspond to a rock failing due to some force, in this case hydraulic fracturing. The rock that breaks is considered to be a more brittle rock/formation compared to those that do not. The surrounding well bore area is the area that was stimulated by hydraulic fracturing where the microseismic events associated with Well 2H cluster around the wellbore.

The microseismic events were measured during fourteen different fracturing stages for the NW trending horizontal well 2H. Only thirteen stages will be considered due to inaccurate coordinate information for the first stage of events. These thirteen stages with the corresponding microseismic events are shown in an aerial view in Figure 4.7. Figure 4.8 shows all stages of microseismic events in a vertical seismic section of $\lambda\rho$-$\mu\rho$. Figure 4.8 shows the events to be clustered about the wellbore. The majority of the events lie within the Lower Barnett, indicative of a more brittle zone. The events abruptly discontinue at the Base Barnett Unconformity suggesting an excellent fracture barrier.

Above the Lower Barnett is the Forestburg, the microseismic events significantly decrease but do not abruptly decrease, as they do at the Base Barnett Unconformity. Henry (2016) attributes this to the lithology of the Forestburg consisting of the massive carbonate beds interbedded with less massive shale and clay stone beds. The lower portion of the Forestburg has a $\lambda\rho$-$\mu\rho$ response similar to the Barnett Shale. The interbedded shales make the lower Forestburg more brittle than the upper portion of the Forestburg formation has more calcite and is thus more ductile. For this reason there are significantly less microseismic events in the upper Forestburg compared to the lower Forestburg.

The microseismic events for stages 2-7 are clustered about the well bore in the Lower Barnett and Barnett Hardshale. However, stages 8-14 closer towards the vertical portion of the well exhibit more diffuse events that the events occur into the lower portion of the Forestburg.

Figure 4.9 extracts $\lambda\rho$ and $\mu\rho$ values for each microseismic event location. As anticipated, most of the events lie in the brittle, less brittle, and less ductile zones (Figure 4.10). However, there is cluster of events corresponding to the ductile region of the brittleness template. Stages 8-14 give rise to events that are less clustered near the heel of the wellbore and located in the limestone Forestburg formation above the Lower Barnett. These un-clustered microseismic events may be due to an increase in pressure when injecting hydraulic fluids near the heel of the well, may be due to some geologic parameter or a combination of both.

Borehole Image Logs

Image logs were used to understand the relationship between microseismic events and event location along the wellbore. Baker Hughes conducted a detailed fracture study using borehole image logs. They concluded the structures or bedding had dip magnitudes of less than 10 degrees with a general south orientation. Five faults were interpreted with no preferred apparent strike direction. 125 open fractures exhibited a general northeast/southwest orientation. 8 shear or induced fractures exhibited no preferred apparent strike direction. 75 cemented fractures exhibited a general northwest/southeast orientation. The open fractures were highly conductive while the closed/partially closed fractures had a much lower conductivity.

Plotting the fracture types along the wellbore (Figure 4.11) the open fracture and partially open fracture intensity is significantly higher towards the heel of the wellbore and decreases towards the toe. The increase in fracture intensity can create a zone of weakness and facilitate the microseismic events to propagate vertically opening these zones of weakness into shallower, less brittle formations.

Fracture Association with the Curvature Attribute

Figure 4.12 shows the most positive curvature attribute overlaid by the seismic amplitude and variance. From Figure 4.11 open and partially open fractures occur in areas with low positive values of the most positive curvature occurring near the heel of the well. Figure 4.13 A and B is a vertical section of the most positive curvature. Non-clustered microseismic events, towards the heel of the well, are correlated to the positive values of the most positive curvature and open fractures. The events appear to be tightly clustered near the more negative or less positive values of the most positive curvature near the mid

portion of the horizontal well path. Near the toe of the well the events that occur in the positive values of the most positive curvature are less tightly clustered compared to the events that occur in the negative part of the most positive curvature and is associated with an increase in open fractures. To conclude, microseismic events are located within the ductile Forestburg limestone formation where there is an abundance of open and partially open fractures that is associated with positive values of the most positive curvature, while events are most clustered around the wellbore in areas with negative values of the most positive curvature containing less open fractures.

A quantitative analysis between positive curvature values and open fractures is shown using a histogram in Figure 4.14. 79% of all the open fractures occur in areas having low positive values (near zero) of most positive curvature. However, open fractures avoid high values of most positive curvature. 19% of open fractures occur in areas with negative values of most positive curvature. There is a significant decrease in open fractures as curvature increases, this will be discussed further in the next section. Additionally, a quantitative analysis was conducted between most positive curvature values and partially open fractures (Figure 4.15).

Curvature Association with the Microseismic Events

Figure 4.15 is a histogram of the extracted most positive curvature attribute values at each microseismic event location. There are a total of 1,397 microseismic event samples with 47% of events associated with curvature values ranging from 0-0.1 and nearly 78% of all events associated with positive values of most positive curvature. However, there is a significant decrease in microseismic events as curvature increases. Microseismic events tend to avoid areas with high curvature values and cluster about areas with low

positive values (near zero) and negative values of most positive curvature, just like in the case of open and partially open fractures. Thompson (2010), found that microseismic activity occurred more often in more negative or near zero values of positive curvature due to sealing of fractures in the ridge like structures. In this study, I find that most of the events avoid areas of high values of positive curvature (Figure 4.16) and cluster about low (near zero) or negative values of positive curvature further supporting Thompson (2010) hypothesis.

Brittleness Classification

A brittleness classification volume was created using a horizon probe with the top of the horizon probe corresponding to the Upper Barnett and the base of the horizon probe corresponding to the Base Barnett Unconformity (Figure 4.17). Microseismic events are clustered within the brittle and less brittle zones apart from the events that occurred in the overlying ductile Forestburg Limestone. The brittleness classification was extracted for every microseismic event location (Figure 4.18). Nearly, 60% of the microseismic events occur in brittle and less brittle zones. The events that occur in the less ductile and ductile zones are primarily in stages (7-14) and correspond to the un-clustered events towards the heel of the well. Figure 4.19 is the brittleness classification extracted at every microseismic event location for stages 2-6, the stages that are more clustered towards the toe of the well. From Figure 4.19 the number of events occurring in the ductile and less ductile regions is significantly less. Nearly 72% of events from stages 2-6 occur in brittle and less brittle regions.

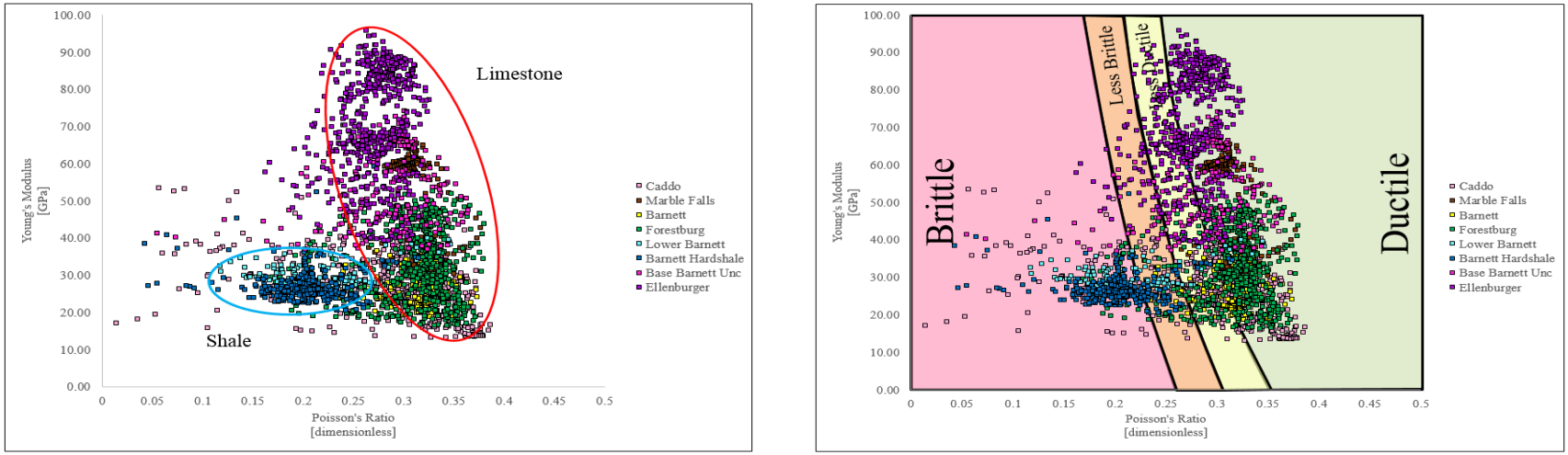

Figure 4. 1: Young's Modulus versus Poisson's ratio plots. (A) All formations in the study. Where the red circle indicates limestone formations while the blue circle indicates shale formations, (B) All formations plotted against Perez and Marfurt's (2013) brittleness template.

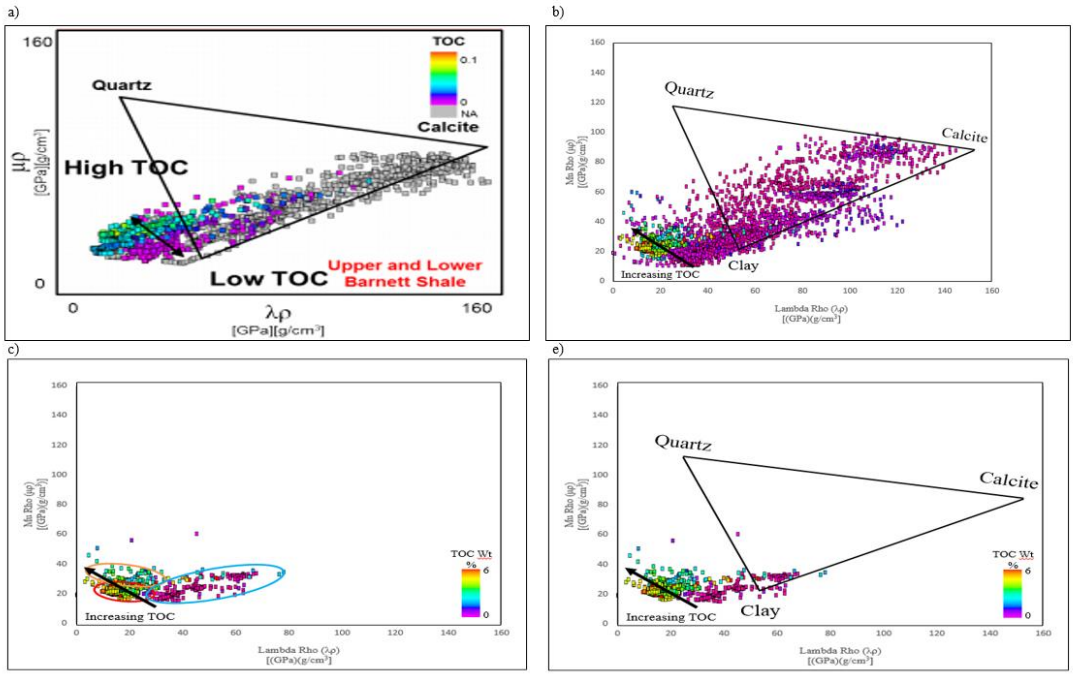

Figure 4. 2: (a) Perez and Marfurt's (2013) TOC values with the overlaying ternary diagram, (b) Modeled TOC values for all formations, (c) Modeled TOC values for only the Barnett Shale. Red circle indicates the Barnett Hardshale, orange circle indicates the Lower Barnett, and the blue circle indicates the Upper Barnett. (d) Modeled TOC of the Upper Barnett, Lower Barnett, and Barnett Hardshale formations overlaid with the ternary diagram.

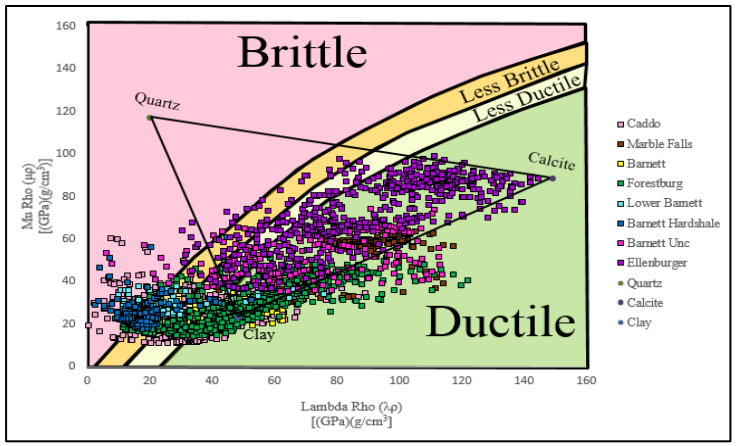

(A)

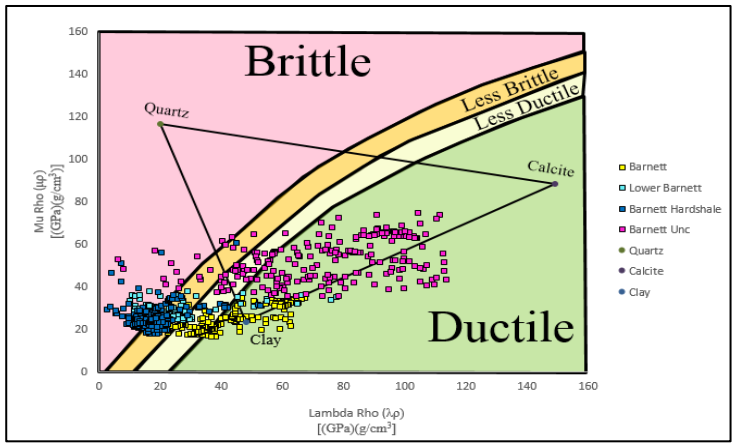

(B)

Figure 4. 3: (A) *λρ-μρ* crossplots of all formations, (B) *λρ-μρ* crossplot for Barnett, Lower Barnett, Barnett Hardshale, and Base Barnett Unconformity with the ternary diagram of the three most common minerals within the Barnett Shale.

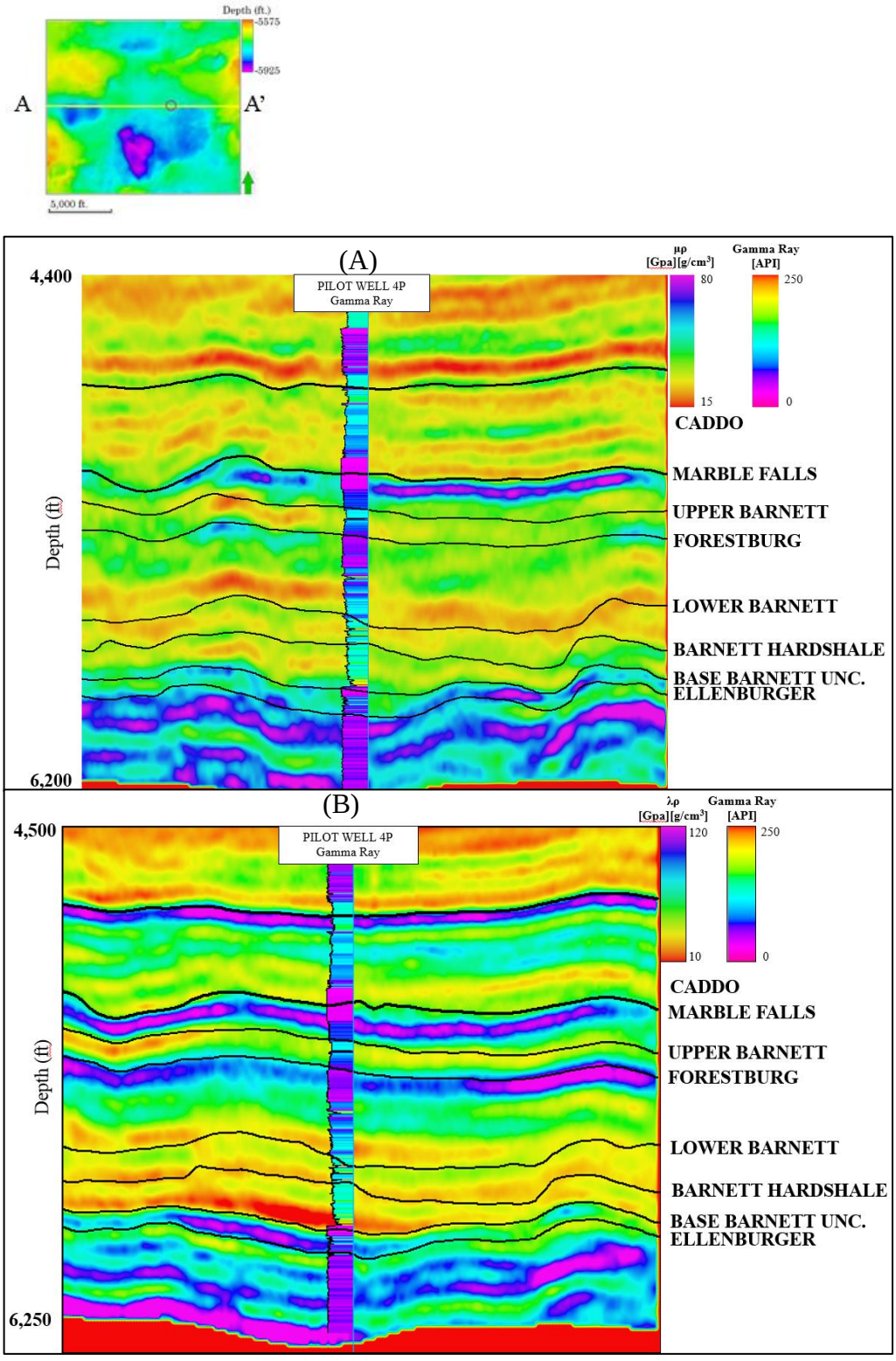

Figure 4. 4: Vertical slices along line AA' through (A) $\mu\rho$ (B) $\lambda\rho$. The well displays gamma ray.

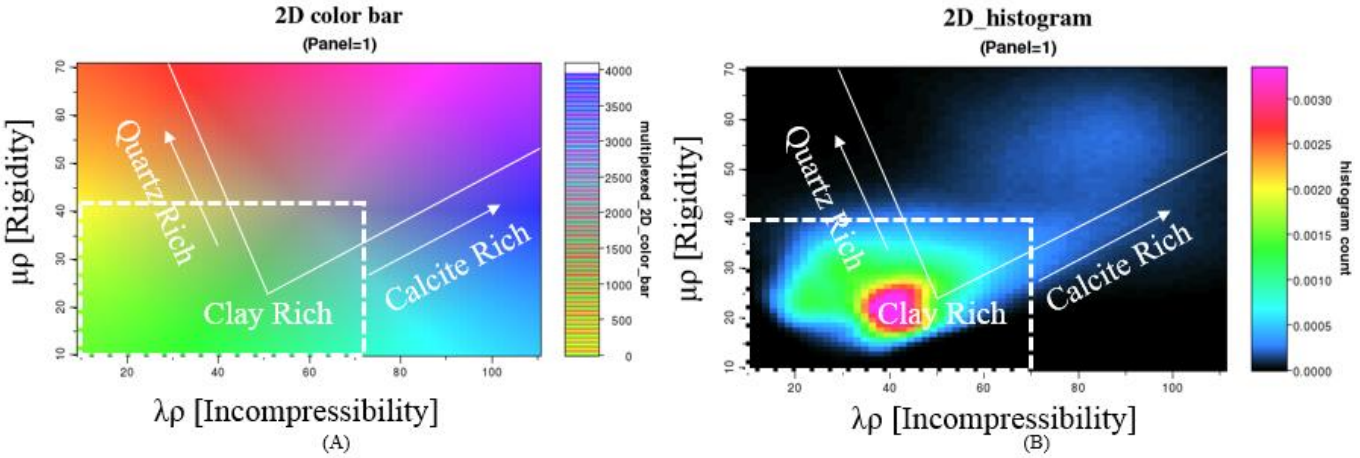

Figure 4. 5: (A) 2D color bar with the ternary diagram in the *λρ-μρ* space, (B) 2D histogram of the data. The white dashed box indicates where the data has been clipped in the following Figures.

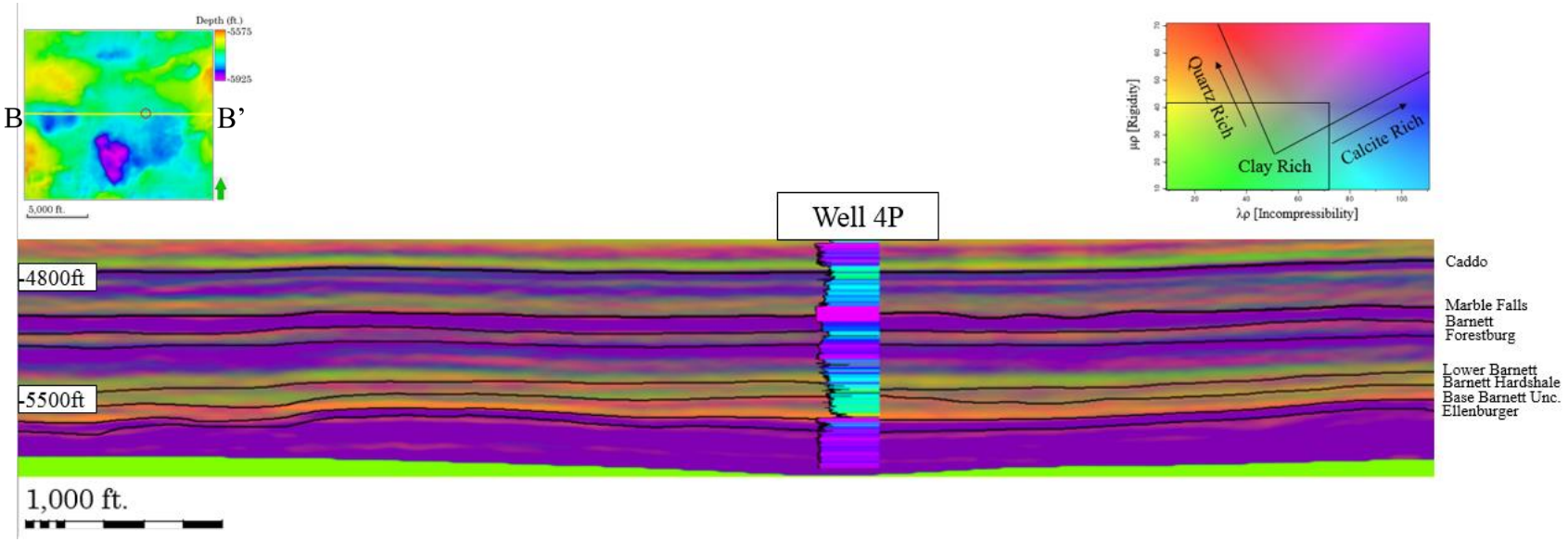

Figure 4. 6: Vertical slice BB' through the *λρ-μρ* cross plot displayed with th gamma ray log from well 4P. Limestone formations appears as purple colors while the shale formations appears as green and yellow colors.

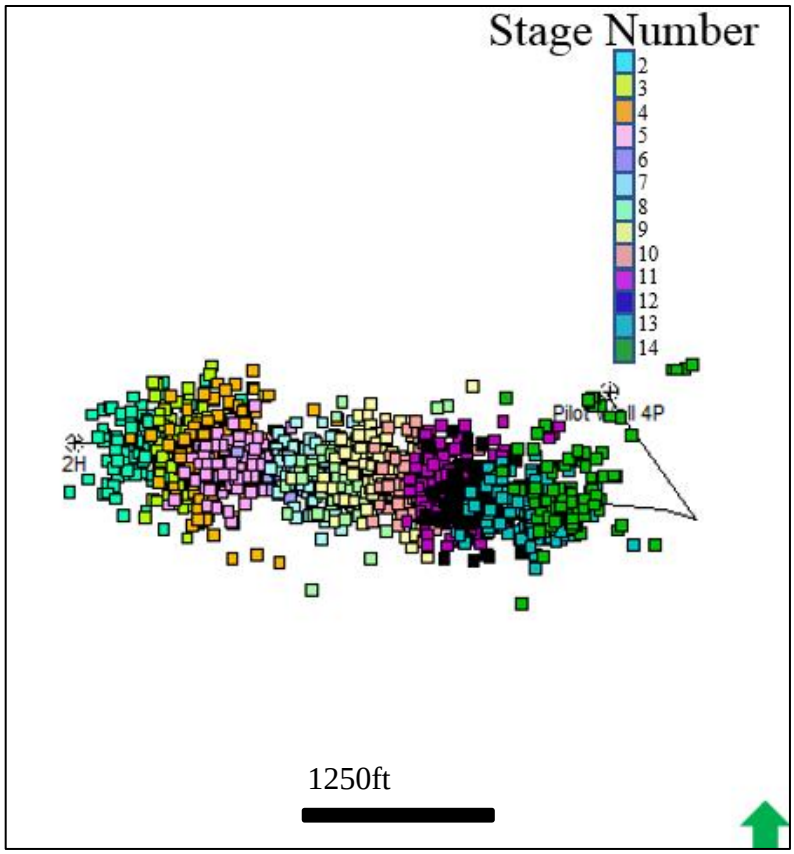

Figure 4. 7: Arial view of the pilot well 4P and the deviated well 2H with its corresponding microseismic events. Different colors represent the 13 different stages

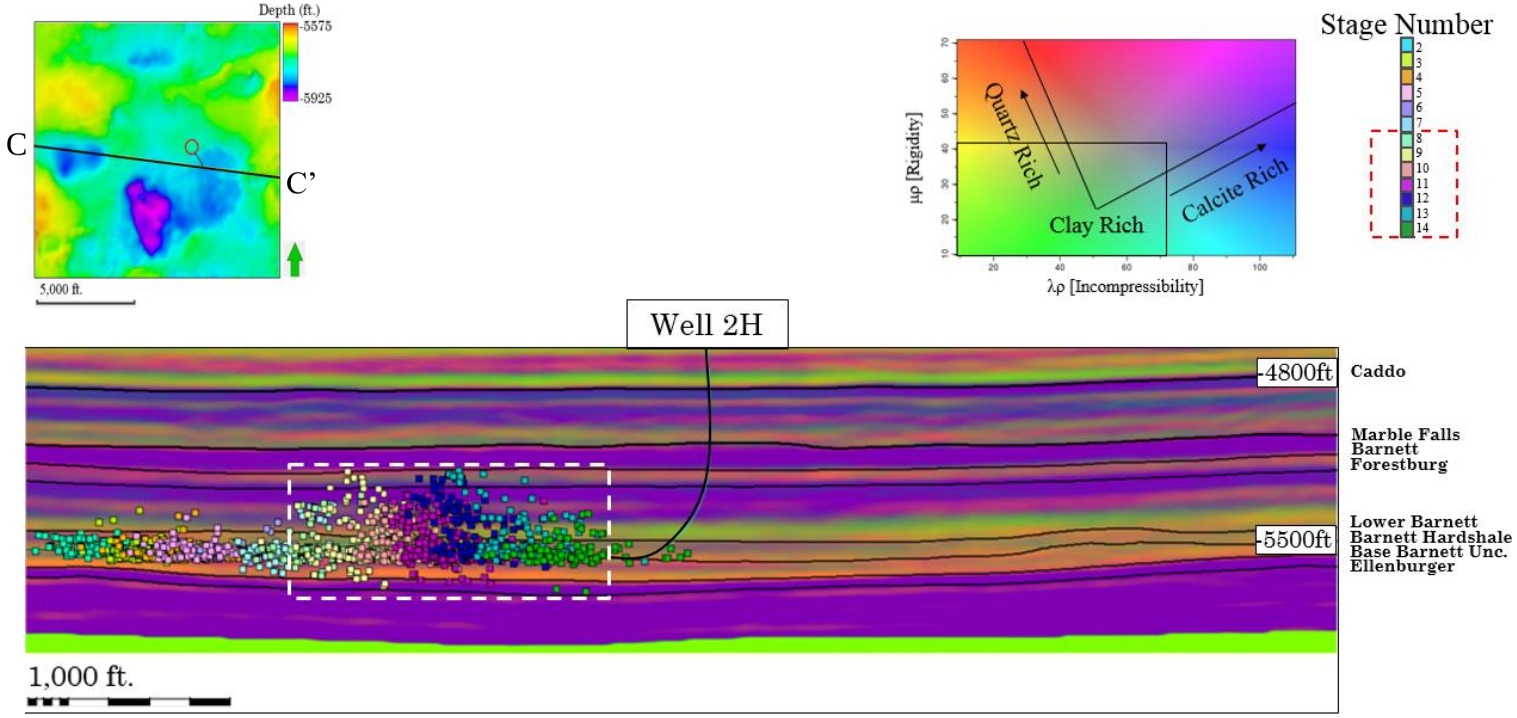

Figure 4. 8: Vertical slice CC' through the $\lambda\rho$-$\mu\rho$ volume along the horizontal path of well 2H, showing the 13 stages of microseismic events corresponding to well 2H. The dashed boxes shows the stages in which the microseismic events are less clustered and propagate into the overlying limestone Forestburg formation.

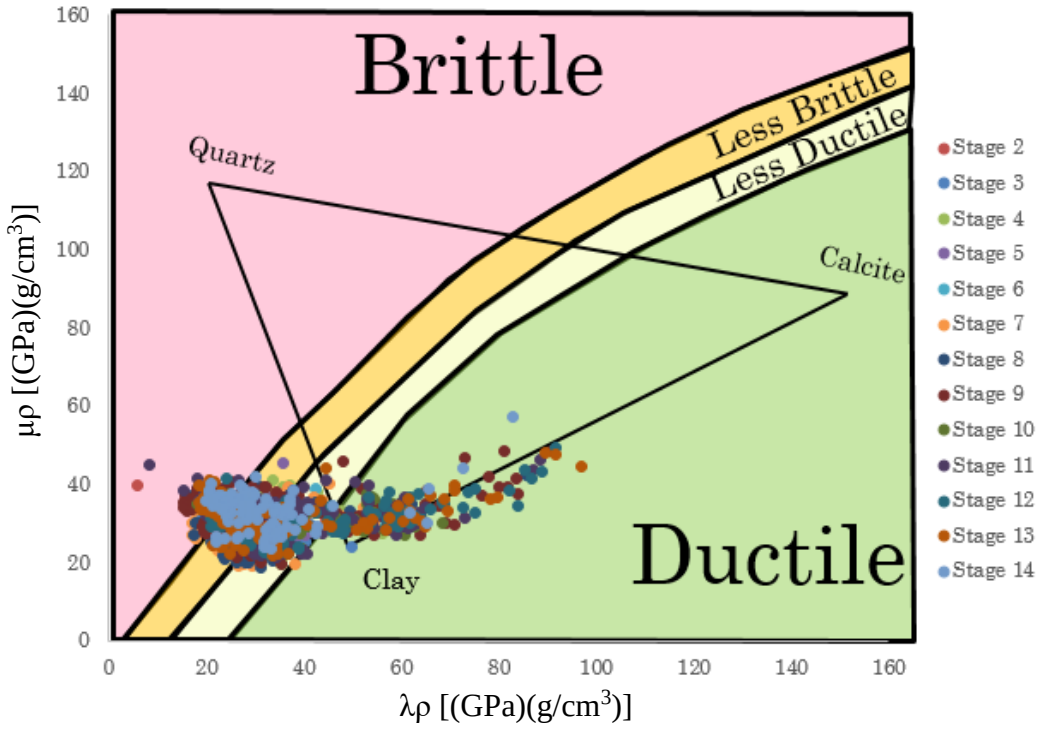

Figure 4. 9: $\lambda\rho$ and $\mu\rho$ values [(GPa)(g/cm^3)] extracted at each microseismic event location for all stages along with the brittleness template and ternary diagram of the three most common minerals in the Barnett Shale.

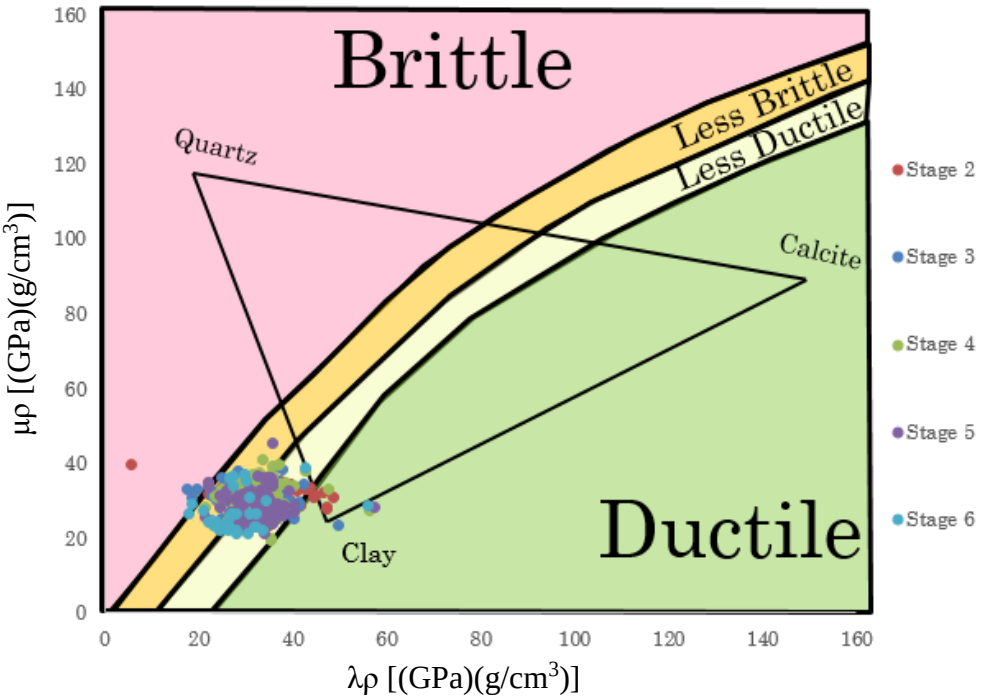

Figure 4. 10: $\lambda\rho$ and $\mu\rho$ values [(GPa)(g/cm^3)] extracted at each microseismic event location for the first five stages along with the brittleness template and ternary diagram of the three most common minerals in the Barnett Shale.

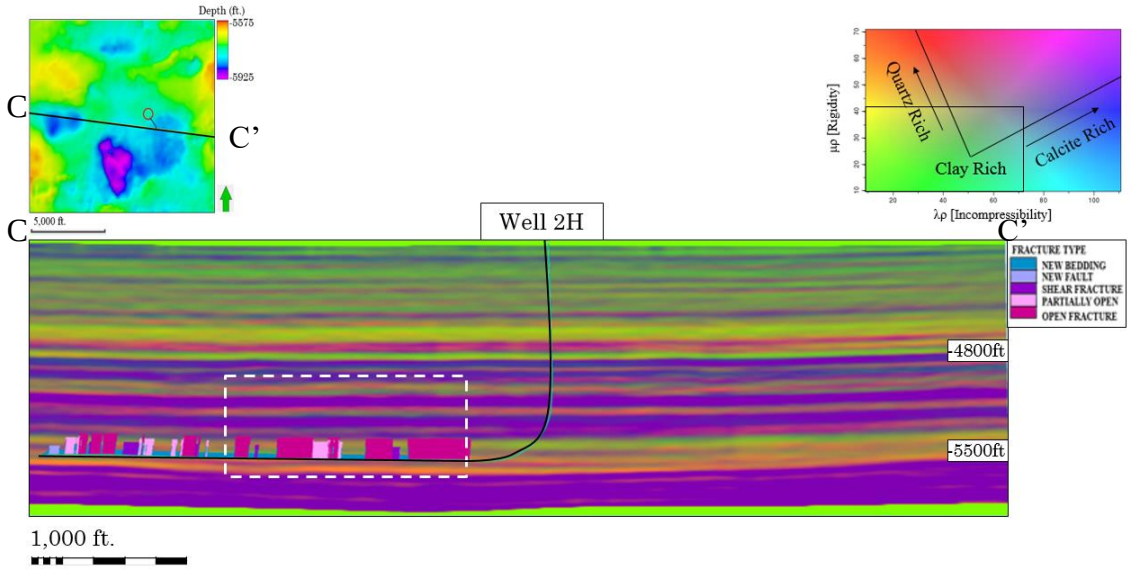

(A)

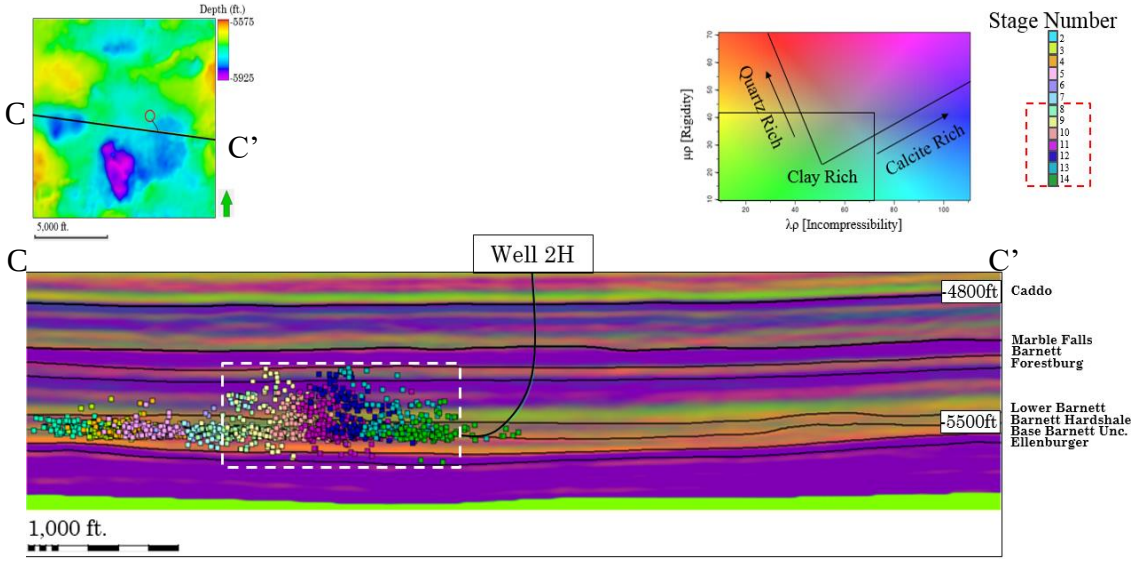

(B)

Figure 4. 11: (A) Vertical slice through the *λρ-μρ* volume with the image log plotted along the borehole of well 2H. White box indicates a zone of more open fractures. (B) Same as A with added microseismic events.

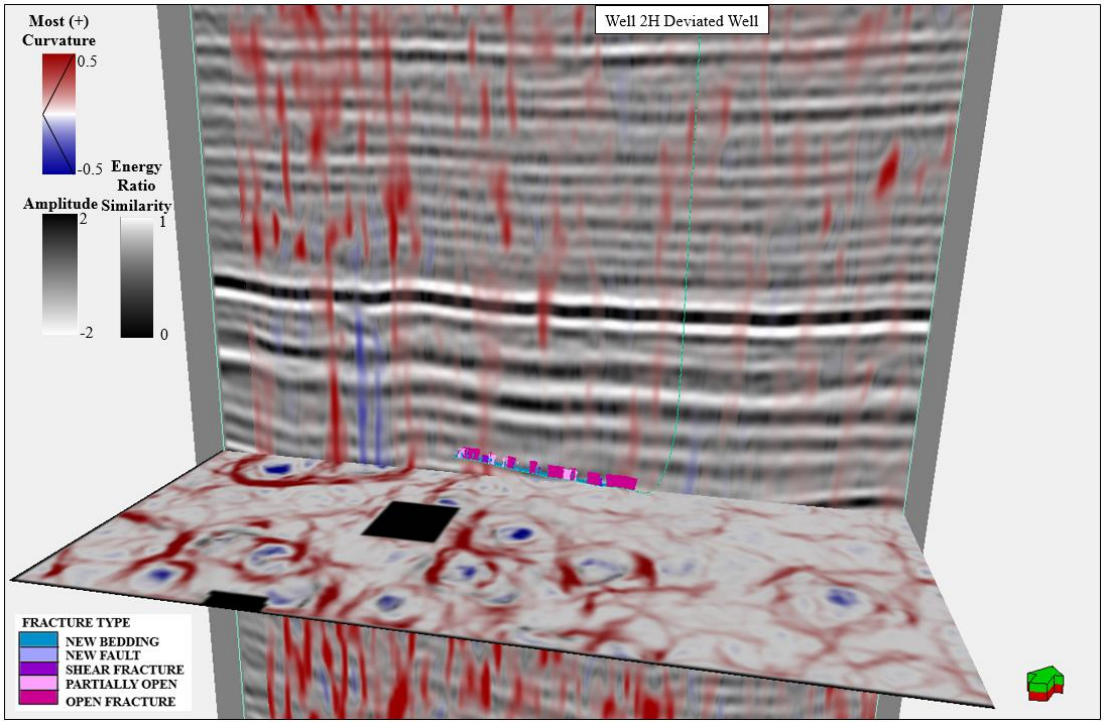

Figure 4. 12: Amplitude data co-rendered with most positive curvature in the vertical seismic section and energy ratio similarity co-rendered with most positive curvature in a time slice. Well 2H displaying the fracture type on the horizontal section of the well. Open fractures are more abundant where a positive curvature anomaly exists.

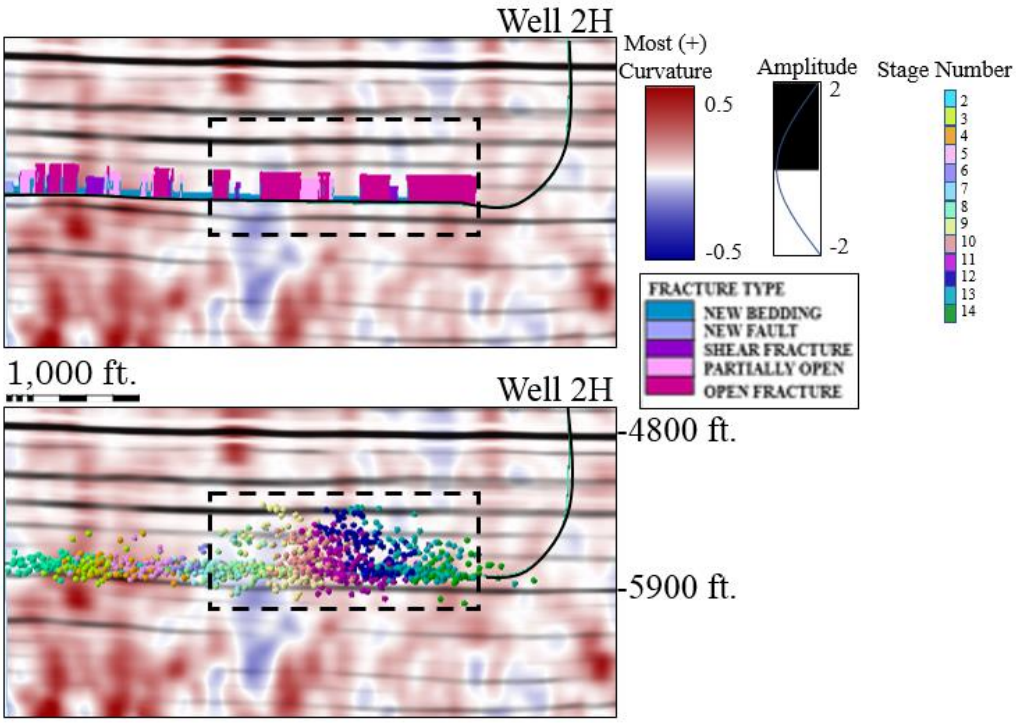

Figure 4. 13: (A) Vertical slice through the most positive curvature co-rendered with seismic amplitude volumes along with well 2H with the corresponding fracture type from image logs, (B) Vertical section of the most positive curvature attribute co-rendered with seismic amplitude along with the 13 stages of microseismic. Black box indicates an area with high open and partially open fracture intensity and un-clustered microseismic events.

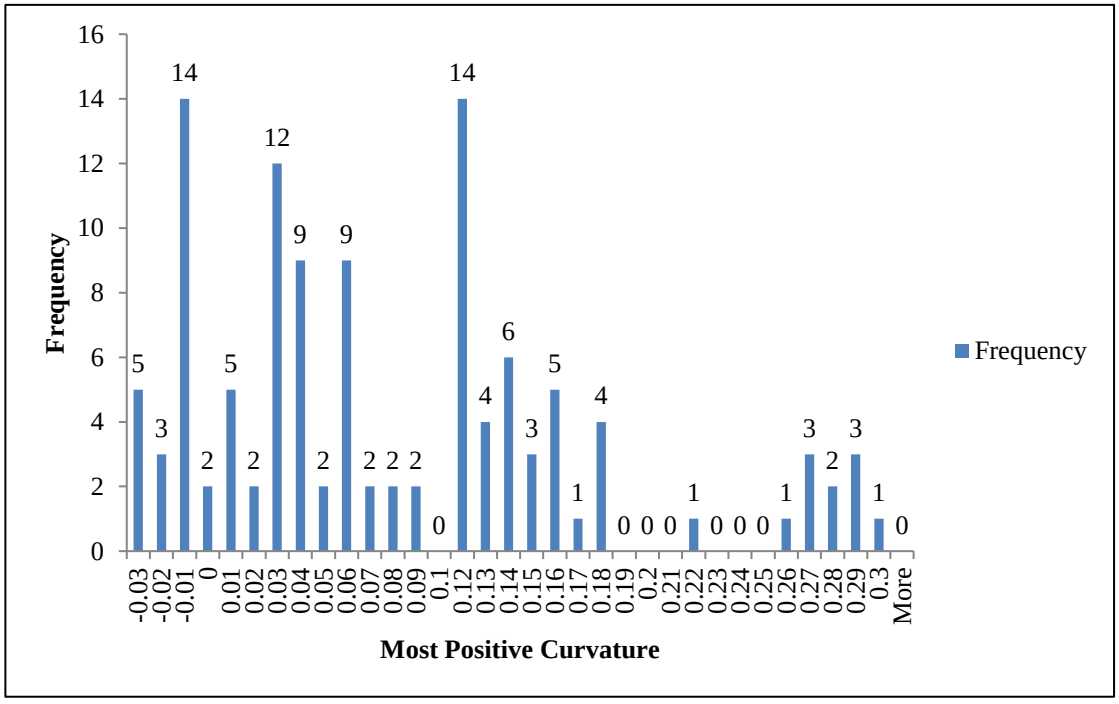

Figure 4. 14: Quantitative analysis of open fractures with associated most positive curvature values.

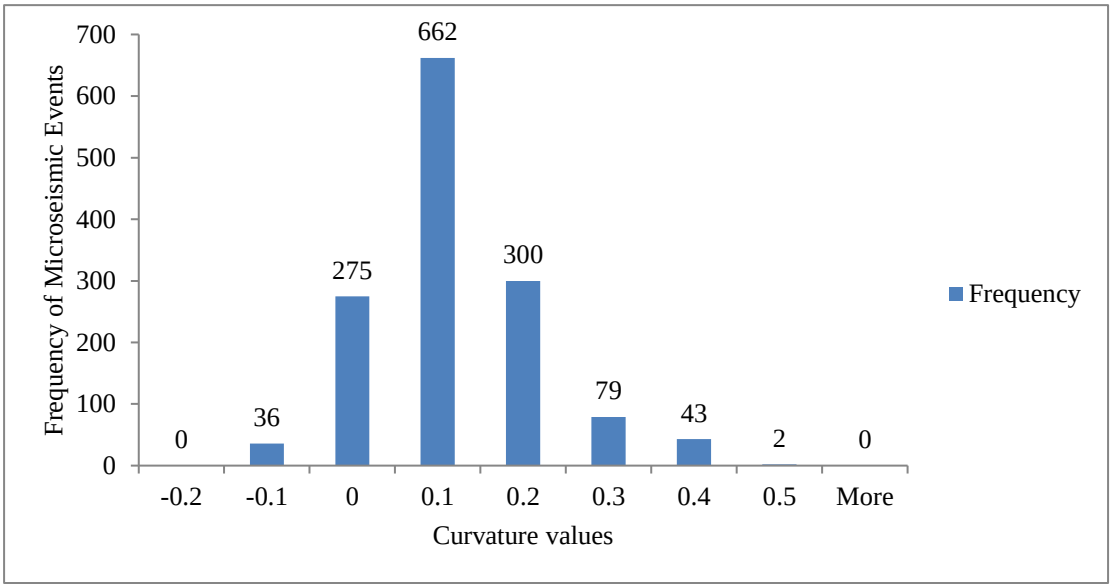

Figure 4. 15: Quantitative analysis of the most positive curvature attribute values for each associated microseismic events.

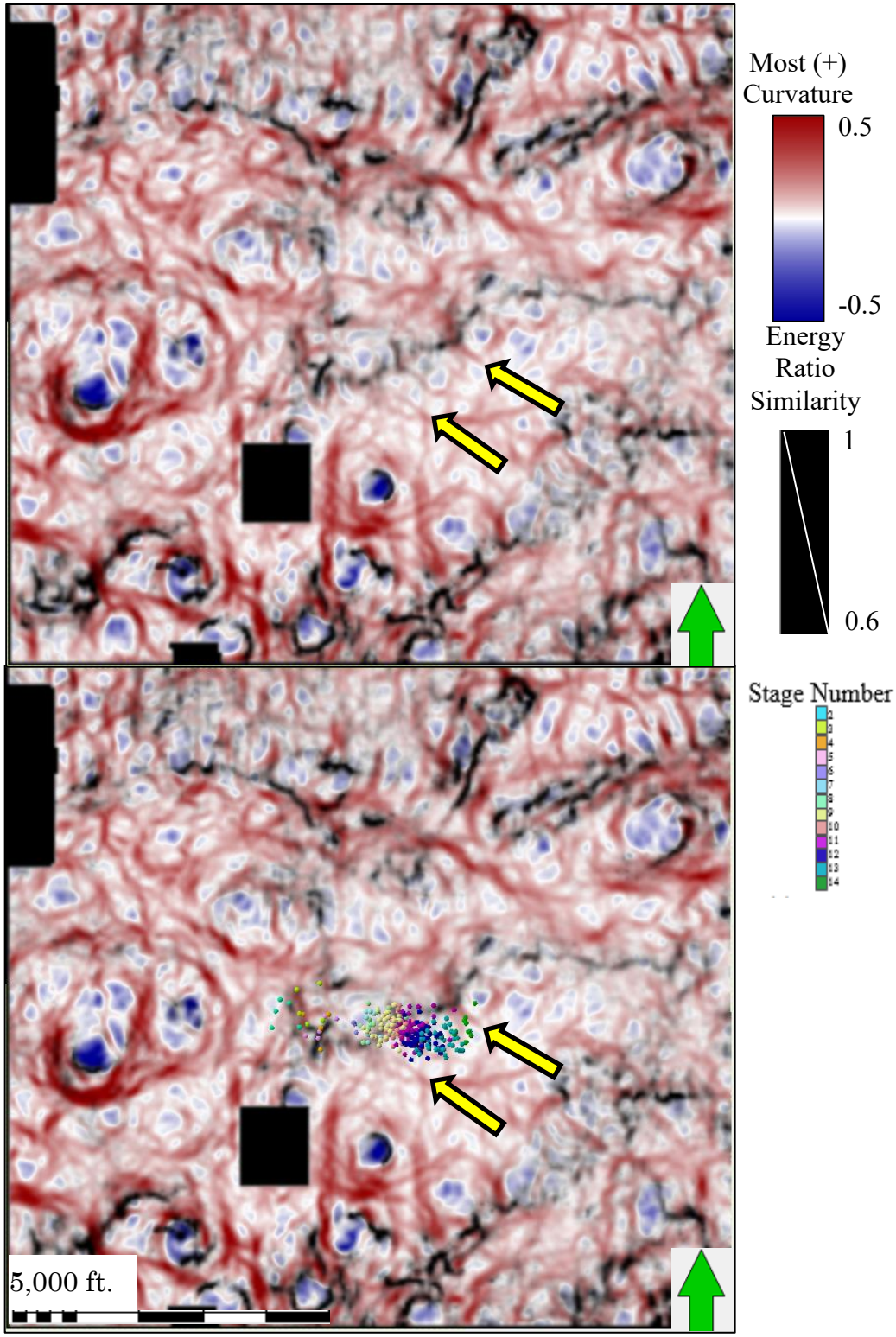

Figure 4. 16: Depth slice of most positive curvature and energy ratio similarity showing the shallower microseismic events. Notice, events avoid areas of higher values of curvature (yellow arrows) and act as fracture barriers and cluster towards lower values and negative dome like features.

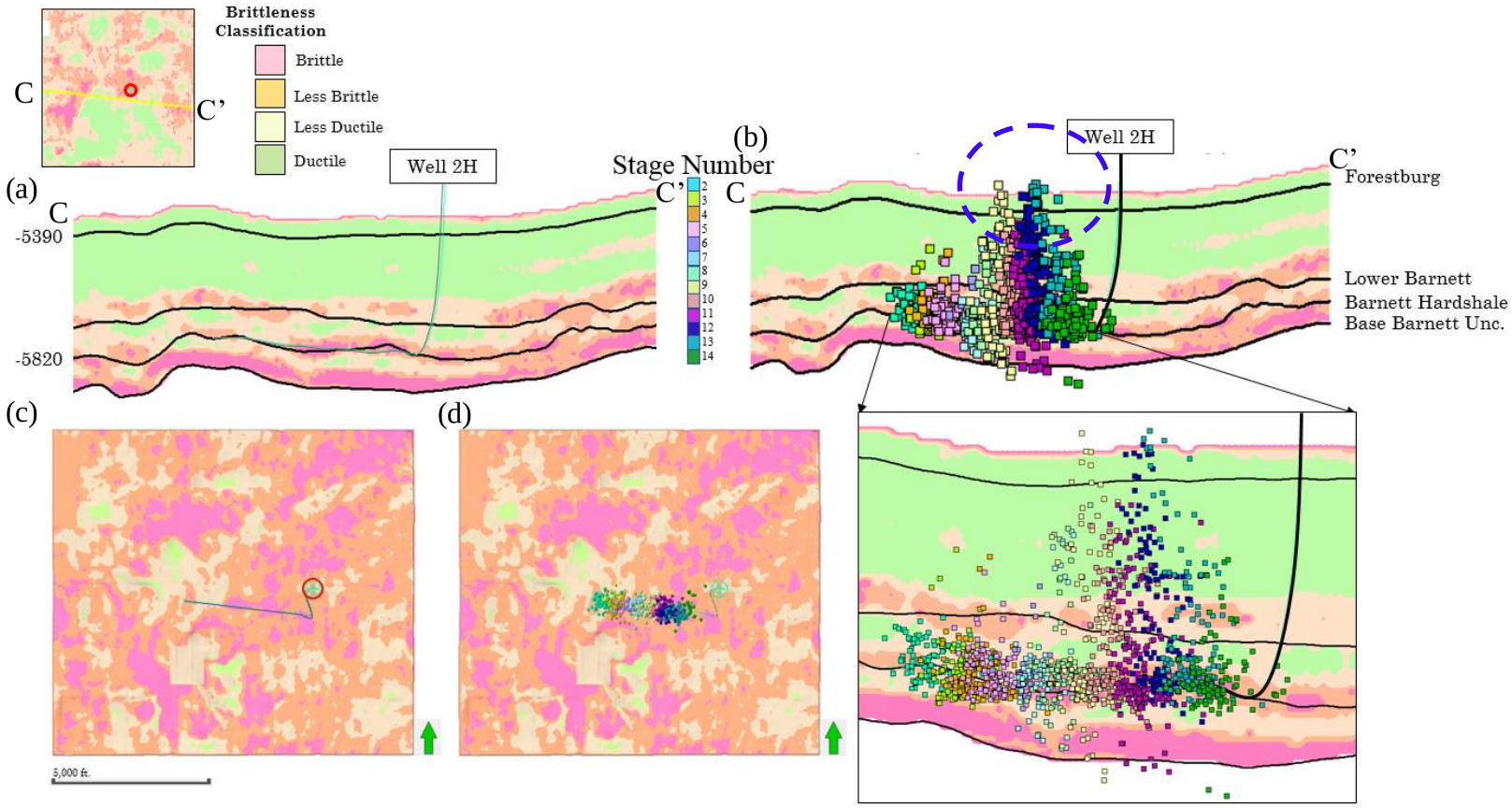

Figure 4. 17: Brittleness classification seismic volume. (a) brittleness classification volume with the well 2H path, (b) same as (a) with the added microseismic events and a close-up section of the microseismic events, (c) horizon slice of the Barnett Hardshale with the well 2H deviated path, (d) same as (c) with the added microseismic events. Many of the events are clustered within the brittle and less brittle zones except for stages 7-14 highlighted by the blue circle which appear in the ductile Forestburg Limestone.

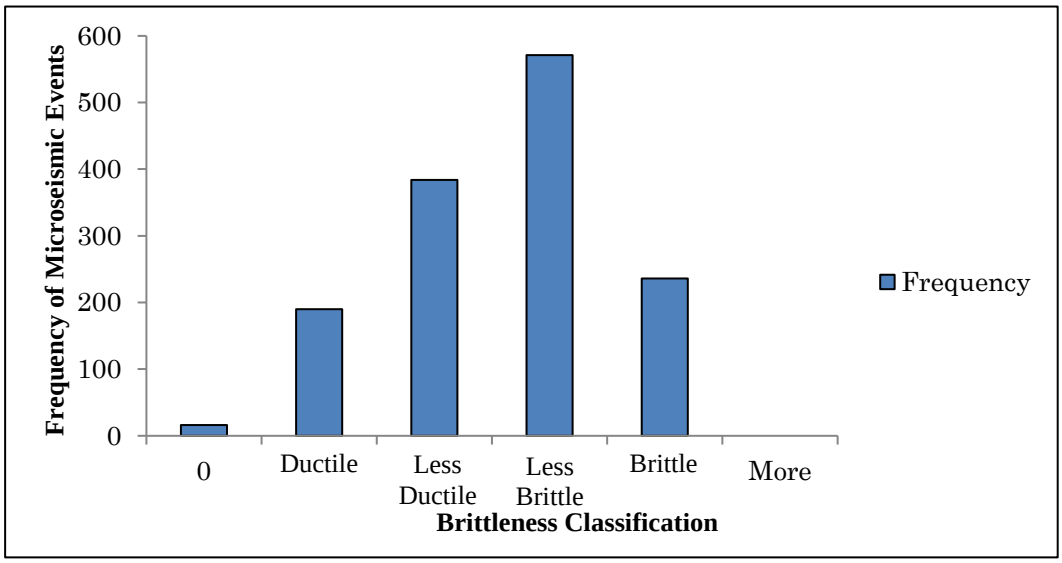

Figure 4. 18: Extracted brittleness classification for every stage of microseismic events at every event location.

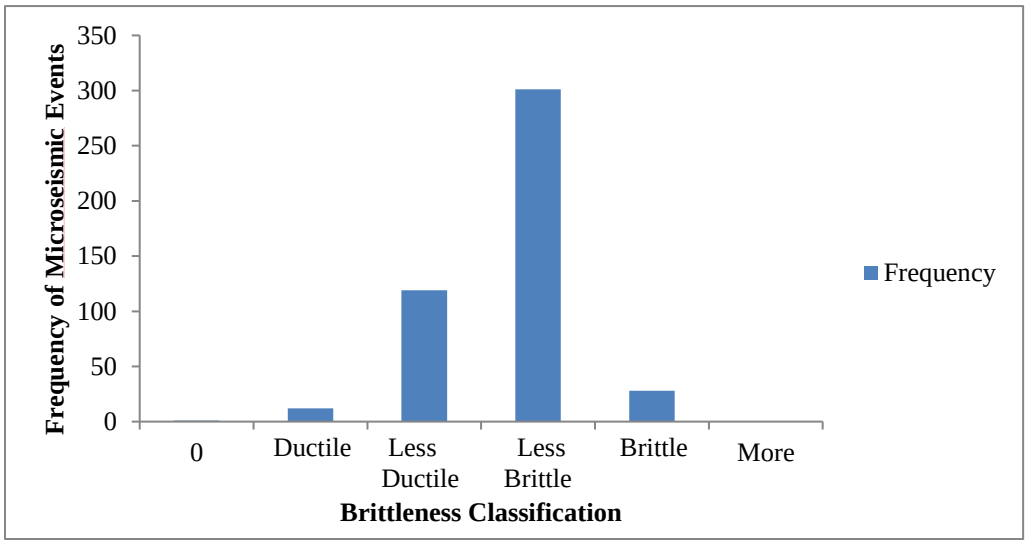

Figure 4. 19: Extracted brittleness classification for stages 2-6 of microseismic events at every event location.

Chapter 5: Conclusions

This study uses well log data, seismic data, microseismic, and borehole image logs to map brittle in a Barnett Shale play. Mineralogy is a major factor when determining brittleness areas. Brittle zones are those with higher quartz and TOC content and appear in the Lower Barnett and the Lower Barnett Hardshale. Ductile zones are clay and calcite dominated and appear in the Marble Falls, Forestburg, and the Base Barnett Hardshale. In this survey, the Lower Barnett is more brittle than the Upper Barnett which has more clay and less TOC content.

With limited well log information, mapping brittle zones was predicted by seismic inversion data and validated by microseismic events. Prestack inversion to calculate $\lambda\rho$ and $\mu\rho$ differentiates brittle and ductile zones. Microseismic events are then used to see where fracture zones are created at each perforation stage, indirectly measuring where the more brittle zones lie. Most microseismic events fall within the targeted, brittle, Lower Barnett and Barnett Hardshale and do not penetrate the Base Barnett Unconformity and Forestburg. In general, the Base Barnett Unconformity and the Forestburg act as ductile fracture barriers which is validated by a lack of microseismic events in both formations. Consistent with other publications on this area.

The further the microseismic events move across the lateral of the well, towards the toe, the more clustered the events become. However, near the heel of the well, the microseismic events became more widespread and less clustered and propagate into the more ductile Forestburg limestone formation. I interpret the previously existing open or partially open fracture networks shown by the borehole image logs form a zone of weakness that allow energy to propagate up and into the Forestburg limestone creating

microseismic events where events are normally not expected to be seen. This should be noted when planning well production and can be economical by decreasing perforation stages when an area is highly fractured. Lastly, 47% of microseismic events occurred where curvature values ranged from 0-0.1 and 78% of microseismic events occurred in areas with positive curvature values. Open fractures are associated with low (near zero) values of positive curvature, supporting Thompson (2010) hypothesis that microseismic activity avoids ridge like structures and trends towards more bowl shapes and low positive values of positive curvature.

References

Bowker, K. A., 2003a, Recent developments of the Barnett Shale play, Fort Worth Basin: West Texas Geological Society Bulletin, **42**, 4 – 11

Bowker, K. A., 2003b, Recent development of the Barnett Shale play, Fort Worth Basin: West Texas Geological Society Bulletin, **42**, no. 6, 1–11.

Bowker, K.A., 2007, Development of the Barnett Shale Play, Fort Worth Basin, AAPG Bulletin, **91**, no. 4.

Cai, M., P.K., Kaiser, and C.D. Martin, 2001, Quantification of rock mass damage in underground excavations from microseismic event monitoring. International Journal of Rock Mechanics and Mining Sciences, **38**, 1135-1145.

Chopra, S., K.J., Marfurt, 2008, Emerging and Future Trends in Seismic Attributes, The Leading Edge, **27**, 3, 298-318.

Cook, J., R.A.,Frederiksen, K., Hasbo, S., Green, A., Judzis, J.W., Martin, R., Suarez-Rivera, J., Herwanger, P.,Hooyman, D., Lee, S., and Noeth, 2007. Rocks matter: Ground truth in geomechanics. Oilfield Review, **19**, no.3, 36-55.

Cook, S., A., Alali, K., Marfurt, and M.,Pranter, M., 2016, Calibrating seismic fracture prediction using borehole image logs, application to the Mississippian limestone. 86th Annual International Meeting of the SEG, Expanded Abstracts, 4023-4027.

Davis, G.H., S.J., Reynolds, 1996, Structural geology of rocks and regions, In Structural geology of rocks and regions, 2nd edition, Wiley.

Donselaar, M.E. and J.M., Schmidt, 2005, Integration of outcrop and borehole image logs for high-resolution facies interpretation: example from a fluvial fan in the Ebro Basin, Spain: Sedimentology, **52**, 1021-1042.

EIA, 2011, Review of emerging resources: U.S. shale gas and shale oil plays.

Goodway, B., T. Chen, and J. Downton, 1997, Improved AVO fluid detection and lithology discrimination using Lamé parameters λρ, μρ and λ μ fluid stack from P and S-inversion: 67th Annual International Meeting of the SEG, Expanded Abstracts, 183-186.

Grieser, B., and J. Bray, 2007, Identification of production potential in unconventional reservoirs: SPE Production and Operations Symposium. Paper #106623.

Hampson, D., 1991. AVO inversion, theory and practice: The Leading Edge, **10**, no.6, 39-42.

Hampson, D.P., B.H., Russell, and B., Bankhead, 2005, Simultaneous inversion of pre-stack seismic data. 75th Annual International Meeting of the SEG, Expanded Abstracts, 1633-1637.

Handin, J., and R. V. Hager, 1957, Experimental deformation of sedimentary rocks under confining pressure: Tests at room temperature on dry samples: American Association of Petroleum Geologists Bulletin, **41**, 50

Handin, J., and R. V. Hager, 1958, Experimental deformation of sedimentary rocks under confining pressure: Tests at high temperature on dry samples: American Association of Petroleum Geologists Bulletin, **42**, 43.

Handin, J., R. V. Hager, M. Friedman, and J. N. Feather, 1963, Experimental deformation of sedimentary rocks under confining pressure: Pore pressure tests: American Association of Petroleum Geologists Bulletin, **47**, 39.

Henry, J., 2016, Barnett-sourced Forestburg provides further opportunity in Fort Worth basin: Oil & Gas Journal, **114**, no. 3, 36-39.

Hill, R. E., 1992, Analysis of natural fractures in the Barnett Shale, Mitchell Energy Corporation T. P. Sims no. 2, Wise County, Texas: Topical report, GRI-92/0094, February, Chicago, Illinois, Gas Research Institute, **50**.

Jarvie, D. M., R. J. Hill, T. E. Ruble, and R. M. Pollastro, 2007, Unconventional shale-gas systems: the Mississippian Barnett Shale of North-Central Texas as one model for thermogenic shale-gas assessment: AAPG Bulletin, **91**, 475 - 499.

Jarvie, D.M., 1991, Total organic carbon (TOC) analysis: Chapter 11: geochemical methods and exploration.

Karastathis, A., 2007, Petrophysical measurements on tight gas shale: M.S. Thesis, Mewbourne School of Petroleum and Geological Engineering: The University of Oklahoma.

Kerans, Charles, 1988, Karst-controlled reservoir heterogeneity in Ellenburger Group carbonates of west Texas, AAPG bulletin, **72**, 1160-1183.

Loucks, R. G., 2008, Origin and modification of Lower Ordovician Ellenburger Group paleokarst breccias and fractures in Central and West Texas, *in* Sasowsky, I. D., C.T., Feazel, J.E., Mylroie, A.N., Palmer, and M.V., Palmer, eds., Karst from recent to reservoirs: Karst Waters Institute, Special Publication, **14**, 130 -135.

Marfurt, K.J. and R.L., Kirlin, 2001, Narrow-band spectral analysis and thin-bed tuning. Geophysics, **66**, 1274-1283.

Mavko, G., T. Mukerji, and J. Dvorkin, 2009, The Rock Physics Handbook: Cambridge University Press.

Maxwell, S.C., J., Rutledge, R., Jones, M., and Fehler, 2010, Petroleum reservoir characterization using downhole microseismic monitoring: Geophysics, **75**, A129-A137.

Montgomery, S. L., 2005, Mississippian Barnett Shale, Fort Worth Basin, NorthCentral Texas: Gas-shale play with multi-trillion cubic foot potential: AAPG Bulletin, **89**, 155 - 175.

Passey, Q. R., S. Creaney, J. B. Kulla, F. J. Moretti, and J. D. Stroud, 1990, A Practical model for organic richness from porosity and resistivity logs: AAPG Bulletin, **74**,1777-1794.

Perez, R., and K., Marfurt, 2013, Mineralogy-based brittleness prediction from surface seismic data: Application to the Barnett Shale: Interpretation 2, no. 4, T255-T271.

Pollastro, R., D. M. Jarvie, R. J. Hill, and C. W. Adams, 2007, Geologic framework of the Mississippian Barnett Shale, Barnett-Paleozoic total petroleum system, Bend arch Fort Worth Basin, Texas: AAPG Bulletin, **91**, 405 – 436.

Qi, J., B., Zhang, K., Marfurt, H., Zhou, and C. Deshuang, 2014. Attribute expression of fault-controlled karst – Fort Worth Basin, TX: 84th Annual International Meeting of the SEG, Expanded Abstracts, 2014, 1522-1527.

Roberts, A., 2001, Curvature attributes and their application to 3D interpreted horizons: First Break, **19**, 85-99.

Russell, B., D. Hampson, and B. Bankhead, 2006, An inversion primer: CSEG Recorder, Special issue, 96-103.

Schmoker, M. J., 1996, Results: The Key to Continuous Improvement.

Singh, P., R., Slatt, and W., Coffey, 2008, Barnett Shale—Unfolded: sedimentology, sequence stratigraphy, and regional mapping.

Staples, E., 2011, Subsurface and experimental analysis of fractures and curvature: M.S. Thesis, U. of Oklahoma.

Stearns III, V. G., 2015, Fracture characterization of the mississippi lime utilizing whole core, horizontal borehole images, and 3D seismic data from a mature field in Noble County Oklahoma: M.S. Thesis, The University of Oklahoma.

Sullivan, E.C., K.J., Marfurt, A., Lacazette, and M., Ammerman, 2006. Application of new seismic attributes to collapse chimneys in the Fort Worth Basin. Geophysics, **71**, no. 4, B111-B119.

Thompson, A. M., 2010, Induced fracture detection in the Barnett Shale, Fort Worth Basin, Texas: M.S. Thesis, ConocoPhillips School of Geology and Geophysics.

Tingay, M., J., Reinecker, and B., Müller, 2008. Borehole breakout and drilling-induced fracture analysis from image logs: World Stress Map Project, 1-8.

Wang, F.P. and J.F., Gale, 2009, Screening criteria for shale-gas systems.

Wells, F., 2004, A new method to help identify unconventional targets for exploration and development through integrative analysis of clastic rock properties: Houston Geological Society Bulletin, **52**, 34 - 49.

Zou, C.N., Z., Yang, S.Z., Tao, X.J., Yuan, R.K., Zhu, L.H., Hou, S.T., Wu, L., Sun, G.S., Zhang, B., Bai, L., and Wang, 2013, Continuous hydrocarbon accumulation over a large area as a distinguishing characteristic of unconventional petroleum: The Ordos Basin, North-Central China. Earth-Science Reviews, **126**, 358-369.

Appendix

Amplitude versus Offset (AVO)

Amplitude changes from peak to trough or trough to peak within a migrated CMP gather are often due to inaccurate velocity picks and subsequent event misalignment when data processing. However, these changes in amplitude may also be due to an AVO effect due to changes in lithology, hydrocarbons, porosity, and water saturation, and more. To address this possibility, AVO curves were made for each of the formation tops used in this study, with the objective to see if the amplitude changes at offsets greater than 30 degrees were due to geology or to processing errors, such as Figure A1. Figures A1-A7 show AVO curves for the Caddo, Marble Falls, Barnett, Forestburg, Lower Barnett, Barnett Hardshale, Base Barnett Unconformity, and the Ellenburger horizons of this survey.

Figure A2 for the top Marble falls formation shows a type 1 AVO effect, or an increase in amplitude with offset, starting with a high positive amplitude that decreases with offset with a possible phase change at farther offsets. Figure A3 shows the AVO curve for the top Barnett Shale. At near and mid offsets of less than 7,000 ft. there is a type 3 AVO effect, or a decrease in amplitude with offset, starting with a negative amplitude and decreasing to a more negative amplitude. At offsets of roughly 7,000 ft, a significant increase in amplitude occurs. This increase may be due to a significant increase in TOC or caused by normal moveout (NMO) stretching. Observing the gathers at offsets greater than 7,000 ft, there is significant stretching of the gathers, seen by lower frequency with offset. Using these far offset gathers will create significant errors in the inversion, so muting the far offset gathers is necessary to be accurate. Figure A4 shows bifurcation of

the Forestburg formation event. This bifurcation may be due to anisotropy within the Forestburg caused by but not limited to changes in lithology, porosity, and fractures. When computing an inversion, the algorithm assumes isotropy across the seismic traces of the formation of interest, therefore muting the far offset events with bifurcation is necessary to obtain inversion results. Lastly, Figure A5 shows possible tuning effects due to variable thickness of bedforms (Marfurt, 2001).

Further research regarding the AVO possibilities within these formations is possible However, further data conditioning of the prestack gathers is required for accurate AVO and inversion results.

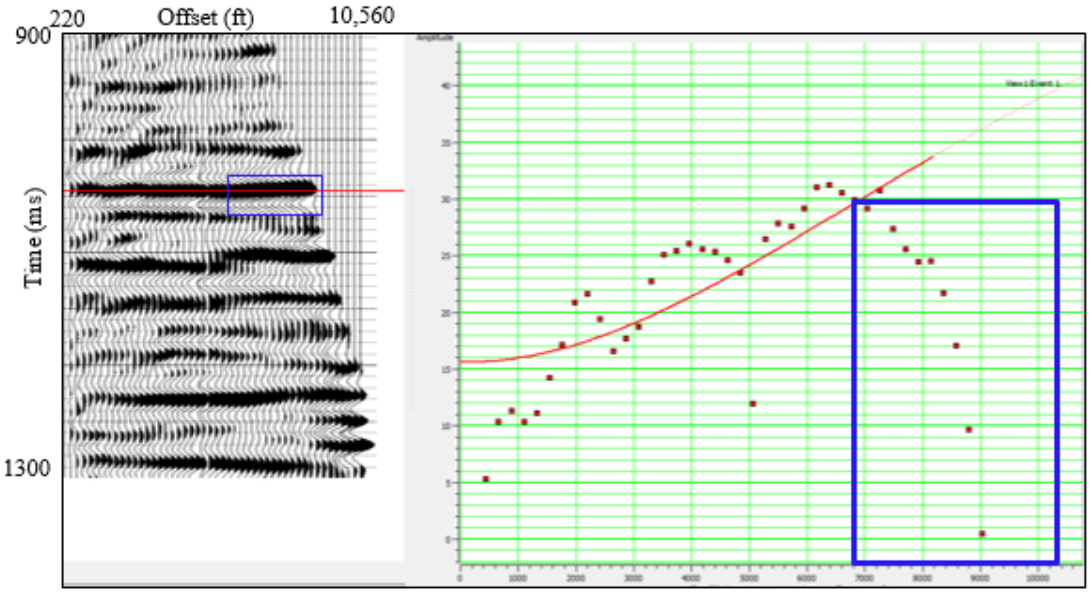

Figure A 1: AVO curve for the Caddo formation. Caddo event is a strong peak across all offsets. The blue box indicates an anomalous area due to near and far offset event not aligned and approaching zero crossing at far offsets, possibly due to slow velocity picks.

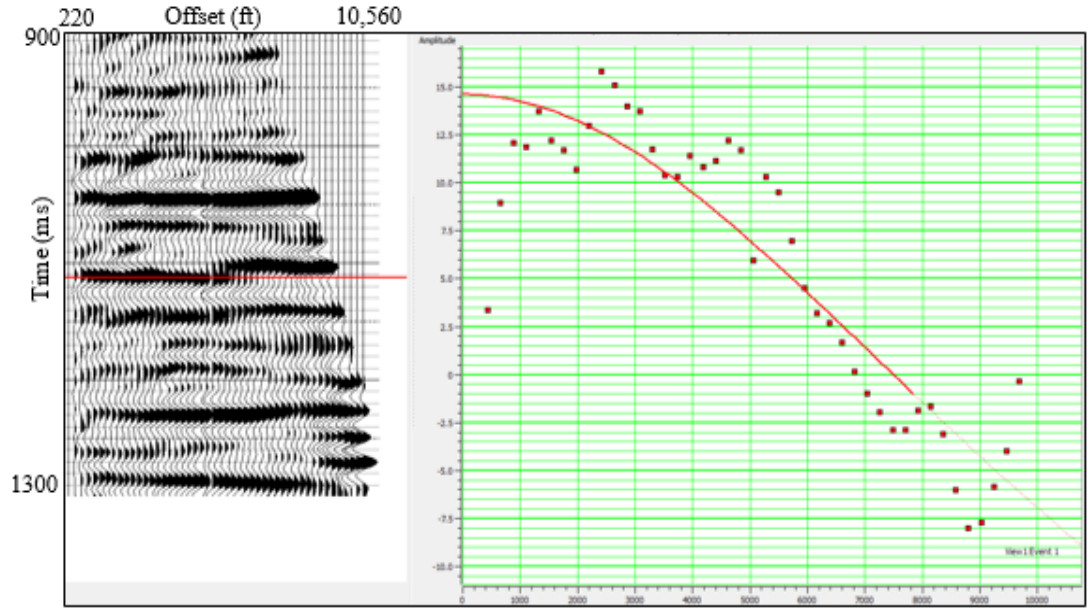

Figure A 2: AVO curve for the top Marble Falls formation demonstrating a type 1 AVO effect.

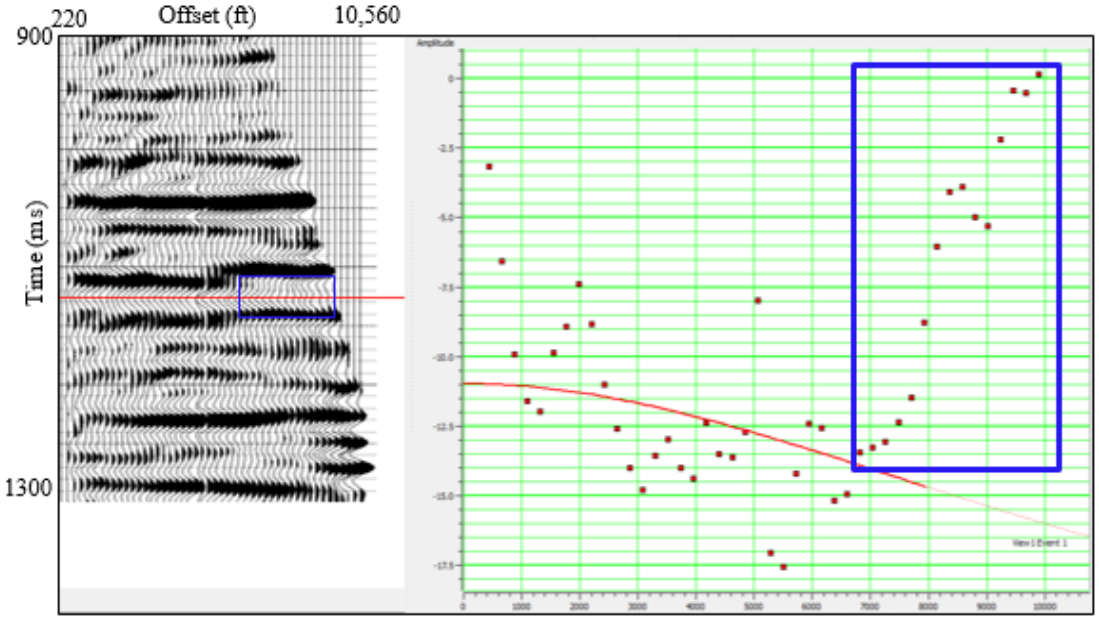

Figure A 3: AVO curve for the top Barnett Shale, the blue box indicates an anomalous area.

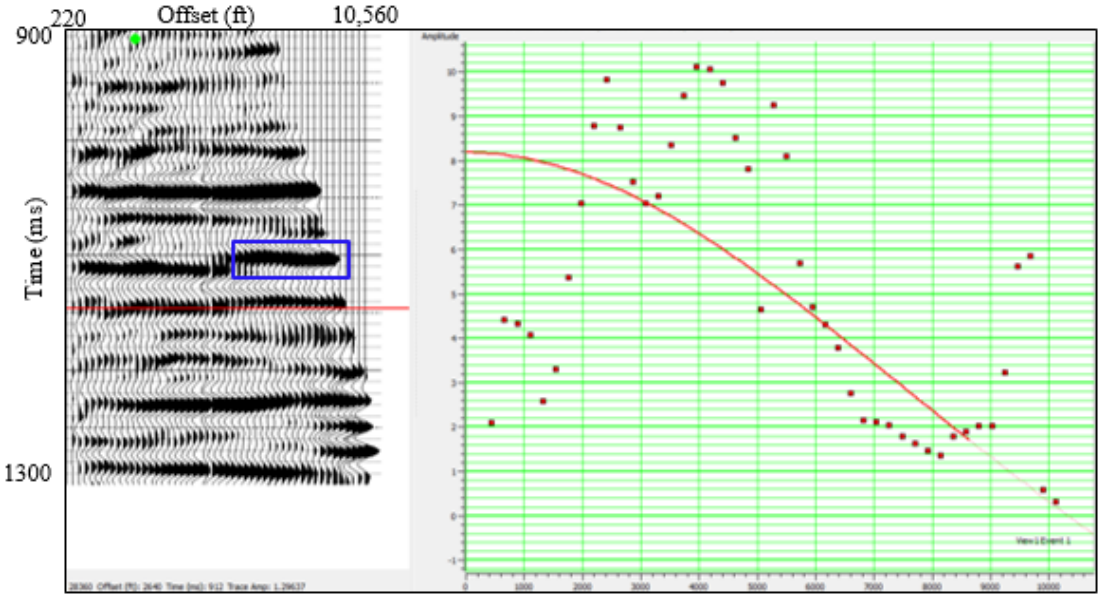

Figure A 4: AVO curve for the Forestburg formation. The blue box indicates an area of interest within the Forestburg formation.

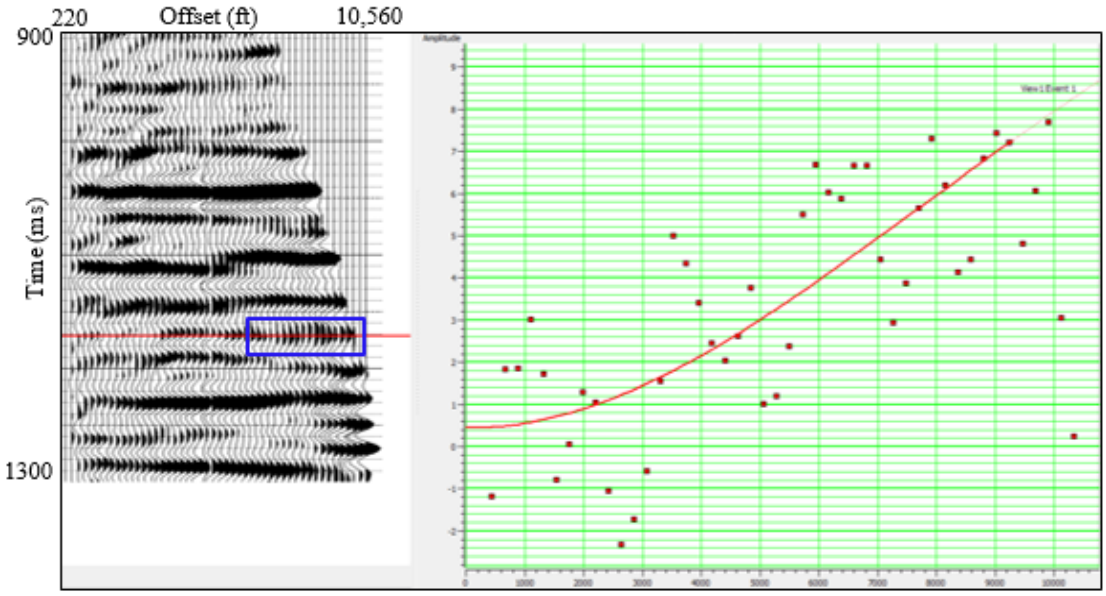

Figure A 5: AVO curve for the Lower Barnett. The blue box indicates possible tuning effects within the Lower Barnett formation.

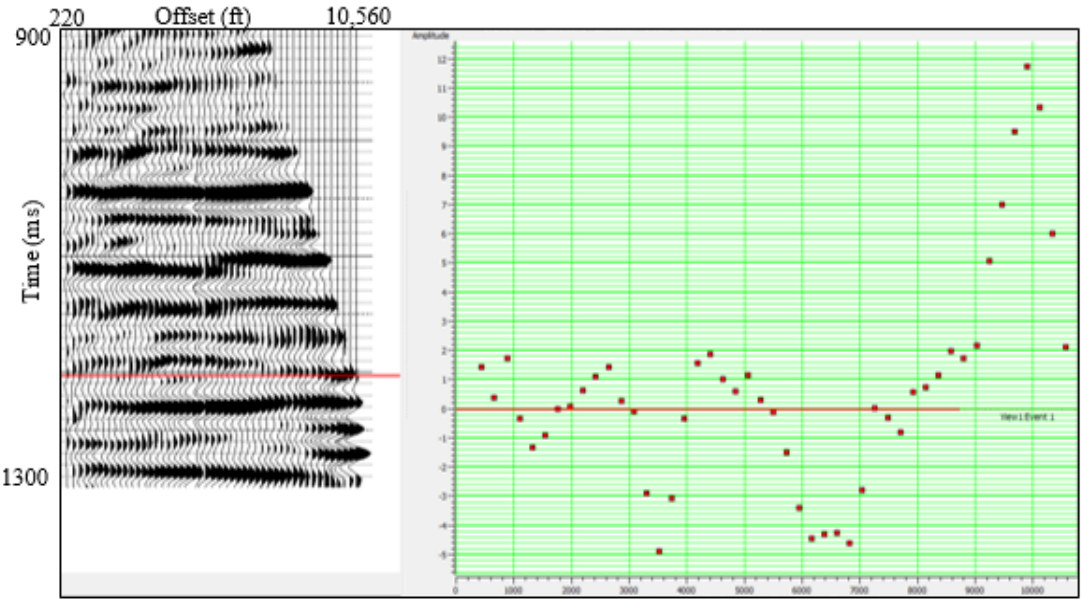

Figure A 6: AVO curve for the Barnett Hardshale formation.

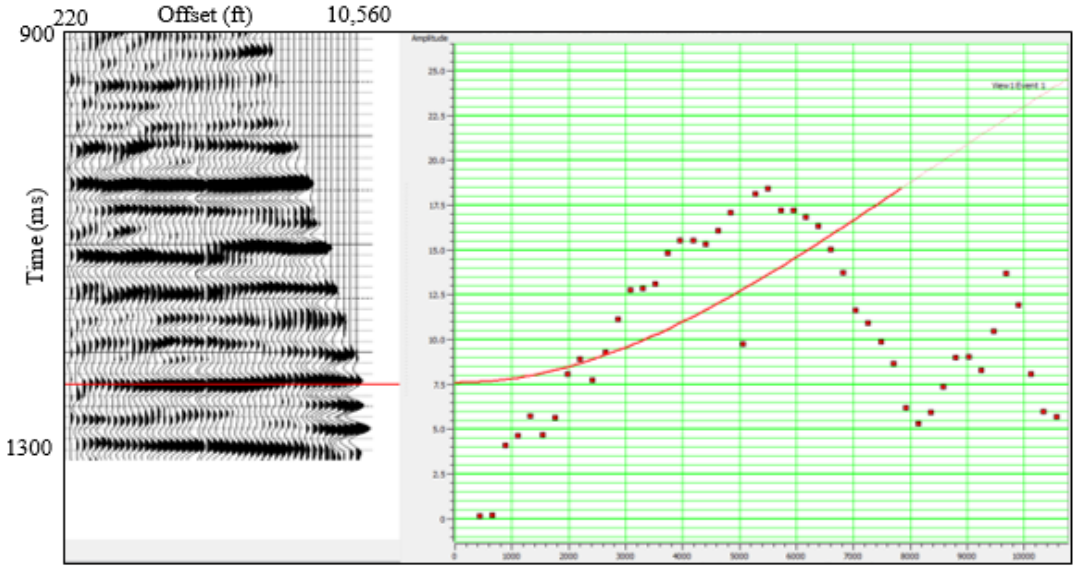

Figure A 7: AVO curve for the Base Barnett Unconformity formation.

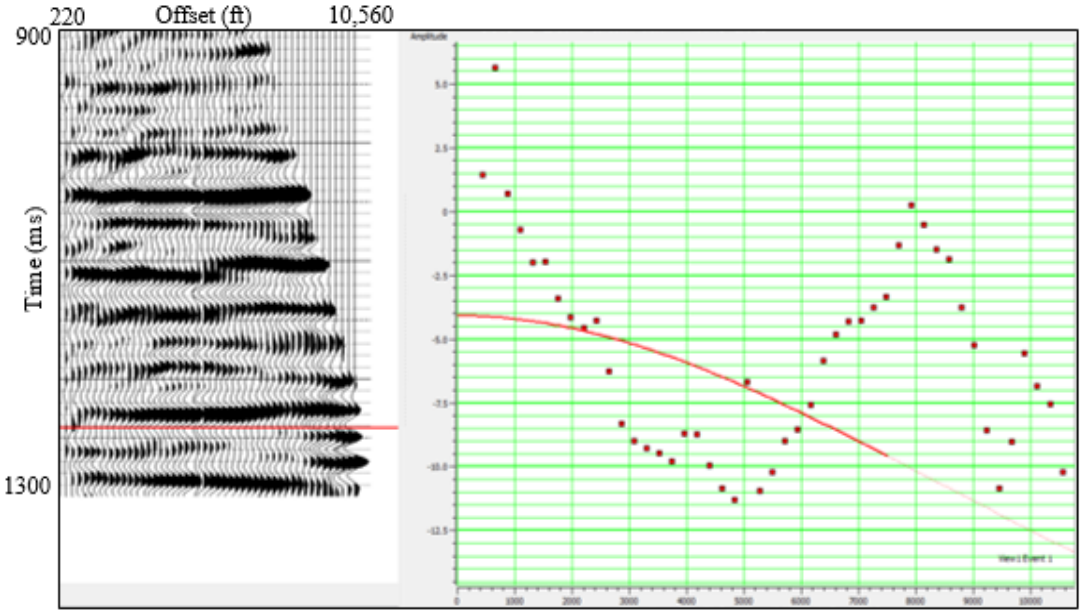

Figure A 8: AVO curve for the Ellenburger formation.